Helsinki University of Technology, Institute of Mathematics, Research Reports

Teknillisen korkeakoulun matematiikan laitoksen tutkimusraporttisarja

Espoo 2005 C018

COMPUTATIONAL PROBLEMS IN PHYSICS 2005
GROUP REPORTS

Timo Eirola **Ville Havu** **Antti-Pekka Jauho** **Jan von Pfaler** **(eds.)**

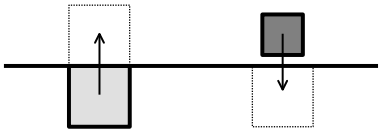

Helsinki University of Technology, Institute of Mathematics, Research Reports
Teknillisen korkeakoulun matematiikan laitoksen tutkimusraporttisarja
Espoo 2005 C018

COMPUTATIONAL PROBLEMS IN PHYSICS 2005
GROUP REPORTS

Timo Eirola Ville Havu Antti-Pekka Jauho Jan von Pfaler (eds.)

Helsinki University of Technology
Department of Engineering Physics and Mathematics
Institute of Mathematics

Timo Eirola, Ville Havu, Antti-Pekka Jauho, Jan von Pfaler (eds.): *Computational Problems in Physics 2005 – Reports*; Helsinki University of Technology, Institute of Mathematics, Research Reports C018 (2005).

Abstract: *This report contains the sub-reports of the working groups of the CPiP 2005 workshop held in Helsinki, Finland, May 23rd - 27th, 2005. The sub-reports are: Group 1: Propagators for Quantum Systems, Group 2: Multiscale Modeling of Epitaxial Growth, Group 3: Markov Chains and Monte Carlo Simulations Without Detailed Balance, Group 4: Electrohydrodynamic Stability Analysis of Two-Phase Flows in Confining Microsystems, Group 5: The Reality of the Compound Solution in Magnetohydrodynamics, Group 6a: A Monte Carlo Approach to DNA-breathing with Two Bubbles, Group 6b: Membranes, Group 6c: DNA knots*

AMS subject classifications: 65-06, 65Z05

Keywords: computational physics, mathematics

Correspondence

Timo.Eirola@tkk.fi, Ville.Havu@tkk.fi, antti@mic.dtu.dk, Jan.von.Pfaler@tkk.fi

ISBN 951-22-7875-8
ISSN 0784-6460

Helsinki University of Technology
Department of Engineering Physics and Mathematics
Institute of Mathematics
P.O. Box 1100, 02015 HUT, Finland
email:math@hut.fi http://www.math.hut.fi/

Contents

Foreword **4**

Group reports **5**

Propagators for Quantum Systems 7

Multiscale modeling of epitaxial growth 23

Markov Chains and Monte Carlo Simulations Without Detailed Balance 33

Electrohydrodynamic stability analysis of two-phase flows in confining microsystems 43

The reality of the compound solution in magnetohydrodynamics . . 53

A Monte Carlo approach to DNA-breathing with two bubbles 63

Membranes 71

DNA knots 77

Participiants **81**

Foreword

The workshop "Computational Problems in Physics" (CPiP) was held in Helsinki, Finland, 23 - 27 May 2005, and this booklet contains the reports by the various projects undertaken during the workshop. The organizers had several goals for arranging the workshop. The first driving force came from their own research experience: it often happens that physicists and numerical analysts tackle similar problems, without knowing of each other's efforts in the area. Physicists may bring "real life" problems to the mathematicians, and mathematicians may have powerful algorithms to solve these problems. The advantages of this cross-fertilization are obvious.

Our hope was then to bring representatives from these two areas together thereby enhancing the chances for these happy encounters. The second main goal was to direct the workshop towards young researchers from both subfields. Skills to communicate to and work together with specialists from a number of different fields are at very high demand, and education towards this direction should start as early as possible. The third goal was to make the students really work together, and not just passively listen to talks given by experts. Therefore a special format for the workshop was deviced, in which work-groups were formed, each working an a specific problem suggested by physicists, and adviced by numerical experts. To make the goals concrete for the work-groups it was decided that each group deliver a short written report about their efforts during the workshop, and this is the final outcome.

The specific projects span a wide spectrum of topics, and we give here a summary in order to introduce the concrete problems discussed in the subsequent sections.

In many different quantum mechanical problems one is concerned with the solution of the time-dependent Schrödinger equation. Thus, Project 1 was defined as "Propagators for quantum systems". Using a physical problem arising from molecular physics a number of propagation models were tested and compared for speed and numerical accuracy. Project 2, "Multiscale modeling of epitaxial growth" had

its origins in a technological problem: in industrial applications one needs thin crystalline films of high quality, and to achieve this, a detailed microscopic understanding of the film growth process is required. Here a diffusion type equation was used to simulate the growth under far-from equilibrium situations, and the stability of resulting structures was analyzed. Project 3, "Markov chains and Monte Carlo simulations without detailed balance" studied the possibility of constructing simulation schemes where the transition rates do not satisfy the detailed balance condition, and analyzed the rate of convergence where certain generalized, alternative conditions are applied. Project 4, "Electrohydrodynamic stability analysis of two-phase flows in confining microsystems", had again a very concrete engineering background: how does an applied electric field affect the stability of the interface between two immiscible liquids flowing in a microchannel? Both analytic and simulation techniques were applied to identify the possible instabilities. Project 5, "The reality of the compound solution in magnetohydrodynamics" dealt with vastly different length scales: here the magneto-hydrodynamic equations relevant for interstellar gas were analyzed; due to their non-strict hyperbolicity a number of special complications arise (for example, uniqueness of the solution is not guaranteed!), which were studied within a one-dimensional code written during the workshop. Finally, Project 6, stemming from biophysics, looked at three sub-tasks: a) Monte Carlo approach to DNA-breathing with two bubbles, b) (Bio) Membranes, and c) DNA knots. A number of simulations were performed, and a whole host of new approaches, algorithms, and untouched problems were identified and discussed, as described in the reports.

As the organizers we are deeply impressed by the depth and range of the projects that the students managed to complete during just a few afternoons and evenings (well, also nights...). Of course this could not have taken place without the dedicated and superbly professional help of all the senior participants, to whom we wish to express our heartfelt thanks, as well as to all our younger colleagues who, without counting working hours, took care of the local infrastructure, and guaranteed a smooth running of the workshop.

In general, this was a very successful workshop, which can be read also from the evaluation forms completed by the participants. Likewise, the senior participants benefitted very significantly from the contacts and discussions with researchers from other fields.

We thank our sponsors NordForsk, Nordita, and Finnish NGSMP for making this first-of-its-kind workshop possible. The viability of our concept and the enthusiasm of the researchers in this type of activity is proven by the fact that another similar workshop with a slightly different focus is already being planned to take place in Sweden in 2006.

Espoo and Copenhagen
September 2005

Timo Eirola
Antti-Pekka Jauho

Group 1
Propagators for Quantum Systems

Dan Bohr, Pablo Cornaglia, Sigríður Sif Gylfadóttir,
Paula Havu, Benny Lassen, Julia Schweitzer, Lasse Tunturivuori

Supervisors:
Marlis Hochbruck, Alexander Ostermann,
Martti Puska, Tapio Rantala

1 Introduction

The problem chosen by our group was to investigate different methods to solve the time propagation of a many-body system in terms of one-electron evolution given by

$$i\frac{\partial}{\partial t}\psi_i(x,t) = \hat{H}\psi_i(x,t), \tag{1}$$

where

$$\hat{H} = -\frac{\nabla^2}{2} + v_{ext}(x,t) + \int dx' \frac{n(x',t)}{|x-x'|} + v_{xc}[n(r,t)], \tag{2}$$

and the electron density of the occupied states is given by

$$n(r,t) = \sum_{i}^{occ} |\psi_i(r,t)|^2. \tag{3}$$

This is the Kohn-Sham Schrödinger equation which is the basic equation of time-dependent density-functional theory (for a review see Ref. [8]).
We decided almost immediately that the Hamiltonian given in equation (2) was too difficult to use as a starting point for the investigation. We chose instead to begin with as simple a Hamiltonian as possible, which still retained some connection with a real quantum mechanical system. This we found in an article by Blanes

and Moan [1]. In this article the following Hamiltonian is proposed to describe the interaction of a diatomic molecule with a laser field:

$$\hat{H} = -\frac{1}{2\mu}\frac{\partial^2}{\partial x^2} + V(x) + xf(t), \quad x \in [-0.8, 4.32], \tag{4}$$

where

$$\begin{aligned} V(x) &= D(1 - e^{-\alpha x})^2, \\ f(t) &= A\cos(\omega t), \end{aligned}$$

and μ is the reduced mass, D the dissociation energy, α the length parameter and A and ω are the amplitude and frequency of the laser field, respectively. As boundary conditions we used two different conditions, Dirichlet and periodic boundary conditions, depending on which was most convenient for the spatial discretization employed. The freedom in choosing the boundary conditions stems from the fact that the only physical requirement on the boundary is that the wave function approaches zero at the boundary (we are only interested in bounded solutions). When imposing periodic boundary conditions we need, of course, to check that the wave function stays away from the boundary. The last thing needed to have a well-posed problem is an initial condition. The usual condition chosen is the ground state of the unperturbed system (time independent, $f(t) = 0$), which is appropriate because we would expect the system to be in the ground state before the laser field is turned on. The only problem with that is that we then needed to find the ground state. Luckily, the ground state is known for the unperturbed problem (Ref. [1]) and is given by

$$\psi_0 = R\, e^{-\beta x} e^{-\gamma e^{-\alpha x}}, \tag{5}$$

where $\gamma = 2D/\omega_0$, $\omega_0 = \alpha\sqrt{2D/\mu}$, $\beta = (\gamma - 1/2)\alpha$, and R is a normalization constant. But even if the ground state was not known there is a rather nice way to find it, provided that the propagation of the unperturbed system (time-independent) can be solved (we needed to solve the propagation of the perturbed system anyway). The idea is to propagate the time independent system in imaginary time, starting with a function that includes the ground state when expanded in the complete set of solutions to the unperturbed system, remembering to normalize the wave function continuously. This will eventually produce the ground state. The reasoning goes as follows:
The starting function was chosen such that

$$\tilde{\psi} = \sum_i c_i \psi_i, \tag{6}$$

where $c_0 \neq 0$ (ψ_0 being the ground state). This can, for example, be achieved by using a multiple step function with random values for each step. The time propagation of this function is known to be given by

$$\tilde{\psi}(t) = \sum_i c_i e^{-iE_i t} \psi_i. \tag{7}$$

So when this function is propagated in imaginary time ($-it$) we see that

$$\tilde{\psi}(-it) = \sum_i c_i e^{-E_i t} \psi_i. \tag{8}$$

It is now evident that as time approaches infinity this function will approach the ground state as long as it is normalized continuously.
In order to fix the material parameters, we chose to look at the HF molecule. The parameters for this system are given in Table 1, where also the amplitude and frequency of the laser field, that we have employed in all calculations, is given. After we had agreed upon the model problem just described we decided to split the

	μ	D	α	A	ω
Values	1745 a.u.	0.2251 a.u.	1.1741 a.u.	0.0011025 a.u.	$0.193 \cdot \omega_0$

Table 1: Material and laser parameters for the system under investigation. Values are given in atomic units (a.u.).

group into three subgroups, where each subgroup was charged with implementing different time integration schemes (methods to solve the propagation of the time-dependent system). The following schemes where chosen:

- Subgroup 1: Splitting of order 2 and 4
- Subgroup 2: Splitting of order 2 and Crank Nicolson
- Subgroup 3: Splitting of order 2 and Magnus integrator of order 2 and 4

The reason why all the subgroups were charged with implementing the splitting scheme of second order was that we then had a way of checking whether or not the different implementations were without errors, they could of course all have the same error, but that would be highly unlikely.
In the following the above mentioned methods will be explained and results of the implementations will be presented.

2 The Crank-Nicolson method

The Crank-Nicolson method was implemented as suggested by Castro *et al.* [2]. Its derivation is as follows: The time-dependent Schrödinger equation has formally the solution

$$\psi(t_1) = \psi(t_0) - i \int_{t_0}^{t_1} \hat{H}(t)\psi(t)\, dt. \tag{9}$$

The integral on the right-hand side is evaluated by the midpoint rule,

$$\psi_1 = \psi_0 - ih\, \hat{H}\left(\frac{t_0 + t_1}{2}, \frac{\psi_0 + \psi_1}{2}\right), \tag{10}$$

where $h = t_1 - t_0$. Here we have introduced the notation $\hat{H}(t, \psi(t)) = \hat{H}(t)\psi(t)$. Further, in the general case with a nonlinear Hamiltonian, $\hat{H}\psi = \hat{H}(t, \psi)$, the Hamiltonian is approximated to

$$\hat{H}\left(\frac{t_0 + t_1}{2}, \frac{\psi_0 + \psi_1}{2}\right) \approx \frac{1}{2}\left(\hat{H}(t_0, \psi_0) + \hat{H}(t_1, \psi_1)\right). \tag{11}$$

In the simple case with only a Morse potential and a laser field, as we have in (4), this relation is exact. For the $(n+1)$:st step, this results in

$$\left(\mathrm{Id} + \frac{ih}{2}\hat{H}\left(t + \tfrac{h}{2}\right)\right)\psi_{n+1} = \left(\mathrm{Id} - \frac{ih}{2}\hat{H}\left(t + \tfrac{h}{2}\right)\right)\psi_n, \tag{12}$$

where Id is the identity operator, $\mathrm{Id}\psi = \psi$. It is easily checked that this method is unitary. Furthermore, the method is also symmetric.

The kinetic term of the Hamiltonian is approximated with finite differences. Let us divide the x-axis into $N+1$ points, all equally spaced with the spacing k. The second derivative of $\psi^m = \psi(x_m)$ is approximated as

$$\frac{\partial^2 \psi^m}{\partial x^2} \approx \frac{\psi^{m+1} - 2\psi^m + \psi^{m-1}}{k^2}, \quad m = 1, \ldots, N-1. \tag{13}$$

We choose Dirichlet boundary conditions, $\psi(x_0) = \psi(x_N) = 0$ in this method, which gives

$$\frac{\partial^2 \psi^1}{\partial x^2} \approx \frac{-2\psi^1 + \psi^2}{k^2} \quad \text{and} \quad \frac{\partial^2 \psi^{N-1}}{\partial x^2} \approx \frac{\psi^{N-2} - 2\psi^{N-1}}{k^2}. \tag{14}$$

In coordinate space, the kinetic term is, thus, represented by a tridiagonal matrix. Further, in this space, the potentials have a diagonal representation, whence the total Hamiltonian sums up to a tridiagonal matrix. This makes the linear system (12) rather easy to solve compared to a system with a full matrix.

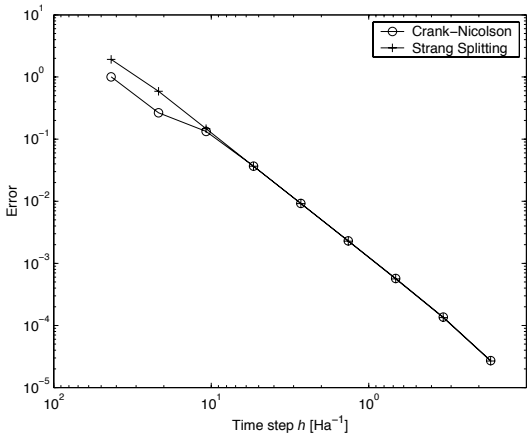

Figure 1: The convergence of the Crank-Nicolson scheme with respect to the time step, compared to Strang Splitting.

The convergence of the Crank-Nicolson method is compared with Strang splitting in Figure 1. We see that Crank-Nicolson shows second order behaviour, as well as Strang splitting does, and that the errors due to time propagation are very close to those of Strang splitting.

Another source of error is the finite difference grid. It induces an error, which decreases quadratically when the number of grid points is increased, which is shown in Figure 2.

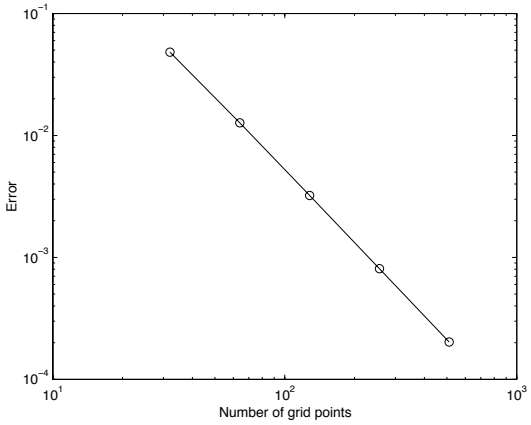

Figure 2: Error of the lowest eigenvalue induced by the finite grid.

3 Exponential Operator Splitting

We consider the time-dependent Schrödinger equation,

$$\frac{\partial \psi(x,t)}{\partial t} = -i\hat{H}(x,t)\psi(x,t) \tag{15}$$

in one dimension. The purpose of this section is to show the split operator approach to solving the time dependence, and in particular consider the symmetric Strang splitting which is of second order, and a simple extension of that method to 4th order.

3.1 Second Order Splitting Methods

Formally the time evolution can be formulated in terms of the time evolution operator re-expressed on a finite time grid t_i as

$$\begin{aligned} \hat{U}(t,0) &= \mathcal{T} e^{-i\int_0^t d\tau \hat{H}(\tau)} \\ &= \prod_{i=0}^{N-1} \hat{U}(t_i + \Delta t_i, t_i), \end{aligned} \tag{16}$$

where $\mathcal{T}$ denotes time ordering and the 'infinitesimal' time evolution operators are

$$U(t_i + \Delta t_i, t_i) = \mathcal{T} e^{-i\int_{t_i}^{t_i+\Delta t} d\tau \hat{H}(\tau)}. \tag{17}$$

Dividing the Hamiltonian into a kinetic part, $\hat{T}$, and a potential part, $\hat{V}$, we face the problem of expressing the exponential of the operator $\hat{H}$. The split operator scheme does this simply by neglecting the fact that $\hat{T}$ and $\hat{V}$ do not commute. The philosophy is that the solution to the complicated differential equation can be approximated by the (hopefully) less complicated partial flows. Neglecting for notational simplicity the spatial dependence of the wave function and focusing only on the time dependence this amounts to considering

$$\begin{aligned} \dot{\psi}(t) &= -i\hat{T}(t)\psi(t) - i\hat{V}(t)\psi(t) \Rightarrow \\ \dot{\psi}_T(t) &= -i\hat{T}(t)\psi_T(t) \rightarrow \psi_T(t+\Delta t) = e^{-i\int_t^{t+\Delta t} dt' \hat{T}(t')}\psi_T(t), \qquad (18) \\ \dot{\psi}_V(t) &= -i\hat{V}(t)\psi_V(t) \rightarrow \psi_V(t+\Delta t) = e^{-i\int_t^{t+\Delta t} dt' \hat{V}(t')}\psi_V(t), \qquad (19) \end{aligned}$$

and thereby the approximation for small time steps Δt

$$\psi(t+\Delta t) \approx e^{-i\int_t^{t+\Delta t} dt' \hat{T}(t')} e^{-i\int_t^{t+\Delta t} dt' \hat{V}(t')} \psi(t), \quad \Delta t \ll 1. \tag{20}$$

The expression in Eq. (20) is in agreement with the infinitesimal time evolution operator in Eq. (17) for time independent Hamiltonians, or for sufficiently small time steps Δt,

$$\int_{t_i}^{t_i+\Delta t} d\tau \hat{H}(\tau) \approx \Delta t \hat{H}(t_i^*), \tag{21}$$

where t_i^* typically is chosen as either an endpoint or the midpoint of the time interval. Thus using the approximation in Eq. (20) we find the time evolution operator

$$e^{-i\int_{t_i}^{t_i+\Delta t} d\tau \hat{H}(\tau)} \approx e^{-i\Delta t \hat{T}(t_i^*)} e^{-i\Delta t \hat{V}(t_i^*)}, \quad t_i^* \in [t_i, t_i+\Delta t]. \tag{22}$$

This approximation is correct to first order in Δt and can be improved considerably by choosing the splitting in a symmetric fashion, the so-called Strang splitting,

$$e^{-i\int_{t_i}^{t_i+\Delta t} d\tau \hat{H}(\tau)} \approx e^{-i\frac{\Delta t}{2} \hat{T}(t_i^*)} e^{-i\Delta t \hat{V}(t_i^*)} e^{-i\frac{\Delta t}{2} \hat{T}(t_i^*)}, \quad t_i^* \in [t_i, t_i+\Delta t], \tag{23}$$

which is correct to second order in Δt.
These splitting schemes are easy to evaluate since we have split the kinetic and potential parts of the Hamiltonian completely, and a diagonal basis can be chosen for each part separately, usually k-space and real space respectively. For instance the Laplacian in Eq. (15) can be solved by Fast Fourier Transformation (FFT), and one then needs to inverse FFT to get back to the real space basis, where $\hat{V}$ is diagonal. The numerical procedure can be illustrated as follows

$$\tilde{\psi}(p, t+\Delta t) = e^{-i\frac{\Delta t}{2}\hat{T}} \texttt{fft}\Big[e^{-i\Delta t \hat{V}} \texttt{ifft}\big[e^{-i\frac{\Delta t}{2}\hat{T}} \tilde{\psi}(p,t)\big]\Big], \tag{24}$$

where $\tilde{\psi}(p,t)$ denotes the Fourier transform of the wave function and where time arguments of $\hat{T}$ and $\hat{V}$ where neglected for notational simplicity. Thus two Fourier transforms are needed at each timestep, making the method scale as $\mathcal{O}(N \log N)$ (slightly superlinearly) with the size of the basis used (e.g. spatial grid). When N is very large, methods which rely on LU factorization of the Hamiltonian matrix, such as the Crank-Nicolson scheme discussed in the previous section, become very slow since they scale as $\mathcal{O}(N^2)$.

3.2 Committed error per time step

Both the standard second order splitting in Eq. (22) and the symmetric splitting in Eq. (23) neglects the commutator $[\hat{T}, \hat{V}]$ as well as higher order commutators. The error committed at each such small time step by each of the above splitting

schemes can be found by simply expanding the exponential and canceling terms (ignoring for simplicity the factor $-i$),

$$\left[e^{\Delta t(\hat{T}+\hat{V})} - e^{\Delta t\hat{T}}e^{\Delta t\hat{V}}\right] \approx \frac{\Delta t^2}{2}\left[\hat{T},\hat{V}\right] + \mathcal{O}(\Delta t^3), \tag{25}$$

$$\left[e^{\Delta t(\hat{T}+\hat{V})} - e^{\frac{\Delta t}{2}\hat{T}}e^{\Delta t\hat{V}}e^{\frac{\Delta t}{2}\hat{T}}\right] \approx \frac{\Delta t^3}{12}\left\{\frac{1}{2}\left[\hat{T},\left[\hat{T},\hat{V}\right]\right] - \left[\hat{V},\left[\hat{V},\hat{T}\right]\right]\right\} + \mathcal{O}(\Delta t^4). \tag{26}$$

Thus the split operator is correct to first order in Δt, while the symmetric Strang Splitting is correct to second order. This provides the rationale for the somewhat strange splitting in Eq. (23).

3.3 Fourth order splitting methods

In the last section we have described Strang splitting, a second order time integration method which uses the fast Fourier transform to simplify the application of the time propagator. Now we will discuss a simple extension of the method to higher orders.

If one has a symmetric splitting method of order $2k > 0$, $\varphi_{2k}(\Delta t)$, e.g. Strang splitting

$$\varphi_2(\Delta t) = e^{-i\hat{T}\frac{\Delta t}{2}}e^{-i\hat{V}(t+\Delta t/2)\Delta t}e^{-i\hat{T}\frac{\Delta t}{2}}, \tag{27}$$

then a symmetric method of order $2k+2$ can be constructed in the following way [9]

$$\phi_{2k+2}(\Delta t) = \varphi_{2k}^n(\alpha\Delta t)\varphi_{2k}^m(\beta\Delta t)\varphi_{2k}^n(\alpha\Delta t). \tag{28}$$

The four parameters α, β, n, m must satisfy two constraints

$$\begin{aligned} 2n\alpha + m\beta &= 1 \\ 2n\alpha^{2k+1} + m\beta^{2k+1} &= 0. \end{aligned} \tag{29}$$

In this splitting scheme, β is always negative, meaning that it involves stepping backwards in time. Although the method is of higher order, it clearly requires more work, since a greater number of steps (3^k) is needed per time step. There exist different splitting schemes of the same order which involve fewer steps (see e.g. [3]), at the cost of having to keep track of all commutators of $\hat{T}$ and $\hat{V}$ up to the order of the method.

Since we have only two constraints for four parameters, two of them can be chosen freely. It has been found [9] that the best choice of m is always $m = 1$, and that the work to achieve a given error decreases with n up to $n = 19$.

In the case where $\varphi_{2k}(\Delta t)$ is given by (27), $k = 1$ and we obtain a fourth order method. In order to keep the implementation simple, we chose $n = m = 1$. Although $n = 1$ is not the best choice, the method involves fewer steps. The wave function at time t is then propagated according to

$$\psi(t + \Delta t) = \varphi_2(\alpha\Delta t)\varphi_2(\beta\Delta t)\varphi_2(\alpha\Delta t)\psi(t). \tag{30}$$

It is a three step process, where each step is identical to that described in the previous section. If an external time dependent potential is included ($\hat{V} = \hat{V}(t)$), it is evaluated at the center of each interval the wave function is propagated by. In this case we would have

$$\begin{aligned}\psi(t + \Delta t) = {} & e^{-i\hat{T}\frac{\alpha\Delta t}{2}} e^{-i\hat{V}(t+\alpha\Delta t+\beta\Delta t+\alpha\Delta t/2)\alpha\Delta t} e^{-i\hat{T}\frac{\alpha\Delta t}{2}} \\ & \times e^{-i\hat{T}\frac{\beta\Delta t}{2}} e^{-i\hat{V}(t+\alpha\Delta t+\beta\Delta t/2)\beta\Delta t} e^{-i\hat{T}\frac{\beta\Delta t}{2}} \\ & \times e^{-i\hat{T}\frac{\alpha\Delta t}{2}} e^{-i\hat{V}(t+\alpha\Delta t/2)\alpha\Delta t} e^{-i\hat{T}\frac{\alpha\Delta t}{2}} \psi(t)\end{aligned} \tag{31}$$

The fourth order splitting requires approximately 3 times as much work as the symmetric Strang splitting. It still scales as $\mathcal{O}(N \log N)$ with the basis size.

3.4 Numerical convergence of implementation

To show the performance of our implementation of the split operator methods, we have in Fig. 3 plotted the deviation from a reference solution (found with a very small timestep) of the wave function ($\epsilon = ||\psi_{\text{ref}} - \psi||_2$) versus the length of the timestep. For reference, the figure includes a straight line corresponding to a second and fourth order decay of the error. The error does decrease according to the order of the methods, although for the fourth order splitting the error decrease slows down at the smallest timesteps. Note that the plot does not show anything about the actual error of the calculation, it only shows the *convergence* of the time evolution.

4 Magnus Integrator for the Schrödinger equation

We are interested in solving numerically the time dependent Schrödinger equation:

$$i\dot{\psi}(t) = H(t)\psi(t), \qquad \psi(0) = \psi_0. \tag{32}$$

In what follows we briefly present the theoretical basis for Magnus Integration using both Krylov subspace decomposition and Padé approximations of the exponential. In the final subsection we comment on the details of our implementation and present the error of the wave function $\psi(t)$ as a function of the integration time step.

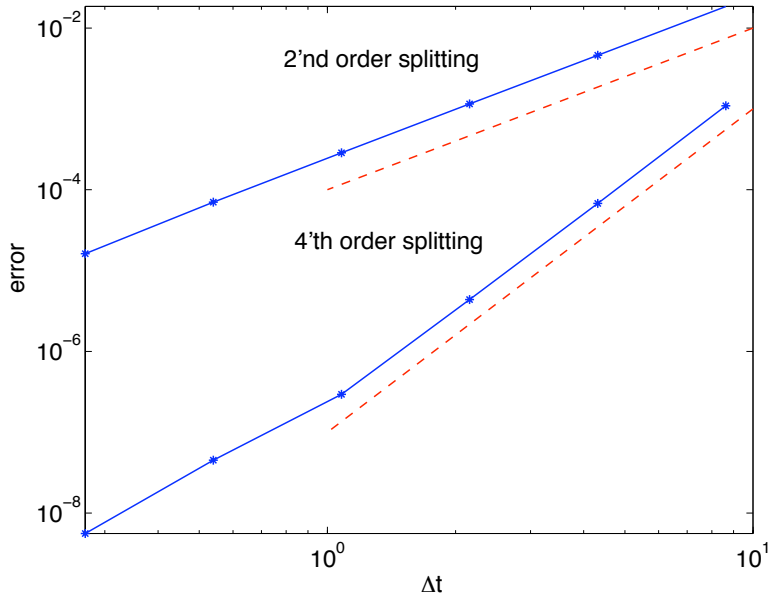

Figure 3: Error of the time evolved ground state wave function with respect to numerical reference solution as a function of timestep length Δt.

4.1 Magnus Integrators

In the Magnus approach [7, 6, 4], the solution of (32) is formally written as

$$\psi(t) = \exp(\Omega(t))\psi_0, \tag{33}$$

for a suitable matrix $\Omega(t)$. If $[H(t_1), H(t_2)] = 0$ for all $t_1, t_2 > 0$ (e.g. if $H(t)$ is scalar), $\Omega(t)$ is simply given by

$$\Omega(t) = -i \int_0^t H(\tau) d\tau. \tag{34}$$

In the general case a differential equation for $\Omega(t)$ can be derived

$$\dot{\Omega}(t) = A(t) - \frac{1}{2}[\Omega(t), A(t)] + \frac{1}{12}[\Omega(t), [\Omega(t), A(t)]] + \cdots, \tag{35}$$

where $A(t) = -iH(t)$.
Solving Eq. (35) using Picard iteration yields the *Magnus expansion*

$$\Omega(t) = \int_0^t A(\tau) d\tau - \frac{1}{2} \int_0^t [\int_0^\tau A(\sigma) d\sigma, A(\tau)] d\tau + \cdots \tag{36}$$

which is convenient for numerical approximations. Different numerical methods can be derived by truncating the series at different points as well as approximating the integrals by using different quadrature rules.
A second order rule is obtained truncating the series in (36) after the first term and using the midpoint rule to approximate the integral:

$$\Omega_n = -i\Delta t\, H(t_n + \Delta t/2) \tag{37}$$

Keeping up to the second term of the right hand side in (36) and using a two-point Gauss quadrature rule yields

$$\begin{aligned}\Omega_n = \quad & -i\frac{\Delta t}{2}\left[H(t_n + c_1\Delta t) + H(t_n + c_2\Delta t)\right] \\ & + \frac{\sqrt{3}\Delta t^2}{12}\left[H(t_n + c_1\Delta t), H(t_n + c_2\Delta t)\right]\end{aligned}$$

where $c_{1,2} = 1/2 \mp \sqrt{3}/6$, which is a fourth order scheme.
The approximation at the new time step $t_{n+1} = n\Delta t$ is then obtained by calculating

$$\psi(t_{n+1}) \approx \psi_{n+1} = \exp(\Omega_n)\psi_n. \tag{38}$$

In the case of unbounded operators $H(t)$, the order statements must be taken with caution. It turns out (for a short review see Ref. [6]) that this method retains fourth order accuracy in the situation $H(t) = T + V(t)$ with T a discretization of the negative Laplacian and $V(t)$ a smooth potential under the time step condition $\Delta t\sqrt{E_{max}} \leq constant$, where E_{max} is the maximum eigenvalue of the Laplacian $E_{max} \sim \Delta x^{-2}$.

4.2 Krylov subspace decomposition

The next step is to calculate the product of the exponential of a matrix times a vector that appears on the right hand side of Eq. (38). An efficient approach for approximation of the product of a matrix exponential times a vector,

$$\psi_{n+1} = \exp(\Omega_n)\psi_n\,, \tag{39}$$

is using the Lanczos process [5, 11]. The symmetric Lanczos process generates recursively an orthonormal basis $V_m = [v_0 \dots v_{m-1}]$ of the m–th Krylov subspace $K_m(\Omega, \psi) = \mathrm{span}(\psi, \Omega\psi, \dots, \Omega^{m-1}\psi)$, such that

$$\Omega V_m = V_m L_m + [0 \cdots 0 \quad \beta_m v_m]. \tag{40}$$

Lanczos Algorithm:	
First iteration:	
$v_0 =$	$\psi/\|\psi\|,$
$w_1 =$	$\Omega v_0,$
$\alpha_0 =$	$w_1^T v_0,$
$v_1 =$	$w_1 - \alpha_0 v_0,$
$\beta_1 =$	$\|v_1\|,$
$v_1 =$	$v_1/\beta_1,$
Following iterations ($i \geq 1$):	
$w_{i+1} =$	$\Omega v_i,$
$\alpha_i =$	$w_{i+1}^T v_i$
$v_{i+1} =$	$w_{i+1} - \alpha_i v_i - \beta_i v_{i-1},$
$\beta_{i+1} =$	$\|v_{i+1}\|,$
$v_{i+1} =$	$v_{i+1}/\beta_{i+1},$

Table 2: Symmetric Lanczos algorithm

The algorithm starts with the starting vector ψ and builds up the orthogonal basis V_m of the Krylov subspace one column at a time. In each step just one matrix-vector multiplication is needed. In the new orthogonal basis V_m the operator Ω is represented by a real symmetric tridiagonal matrix,

$$L_m = \begin{bmatrix} \alpha_0 & \beta_1 & & \\ \beta_1 & \alpha_1 & \ddots & \\ & \ddots & \ddots & \beta_{m-1} \\ & & \beta_{m-1} & \alpha_{m-1} \end{bmatrix}, \tag{41}$$

which is also built up one row and column at a time, using the basic recursion given in Table 2.
The real, tridiagonal, and symmetric matrix $L_m = V_m^T \Omega V_m$ is the orthogonal projection of Ω into $K_m(\Omega, \psi)$. The product of the exponential times the vector is calculated using

$$\exp(-i\Delta t\Omega)\psi \simeq V_m \exp(-i\Delta t L_m)\|\psi\| e_1, \tag{42}$$

where $\|\cdot\|$ denotes the Euclidean vector norm and e_1 is the first canonical unit vector.
The matrix exponential $\exp(-i\Delta t L_m)$ can be computed cheaply using the decomposition $L_m = Q_m D_m Q_m^T$, with D_m diagonal, and

$$\exp(-i\Delta t L_m) = Q_m \exp(-i\Delta t D_m) Q_m^T. \tag{43}$$

The criterion for stopping the Lanczos process is that

$$\beta_m |[\exp(-i\Delta t L_m)]_{m,m}| < tol, \tag{44}$$

where *tol* is a user defined tolerance. This method requires m multiplications of Ω with a vector, where m is in in general much smaller than the dimension of the problem.

4.3 Padé approximations

An alternative way of calculating the exponential is using a rational approximation [10].

$$e^{-z} \approx R_{m,n}(z) = \frac{P_m(z)}{Q_n(z)}, \tag{45}$$

where $P_m(z)$ and $Q_n(z)$ are polynomials of degree m and n with coefficients $\{\rho_k\}$ and $\{\sigma_k\}$ respectively

$$P_m(z) = \sum_{i=0}^{m} \rho_i z^i, \quad Q_n(z) = \sum_{i=0}^{n} \sigma_i z^i \tag{46}$$

The unknown coefficients of $R_{m,n}$ can be determined from the condition that the first $(m+n+1)$ terms vanish in the MacLaurin series

$$Q_n(z)e^{-z} - P_m(z) = 0. \tag{47}$$

Substituting the two polynomials into this expression and equating the coefficients leads to a system of $m+n+1$ linear homogeneous equations which can be solved recursively for the coefficients.

4.4 Implementation and Results

We implemented the second order as well as a fourth order Magnus integrator both by using Krylov subspace decomposition as described in subsection 4.2 and calculating the exponential of the full matrix Ω_n directly. In order to use a Fourier spatial discretization including fast Fourier transforms, we implemented a matrix–free Krylov–subspace algorithm. In the latter case, to calculate the matrix exponential directly we used the *expm* routine of Matlab which uses Padé–approximations and whose implementation corresponds to method 3 of Ref. [10].
For the examples originally studied the time dependence was too weak to be able to obtain the order of the methods. This is due to the fact that the Magnus integration is exact for time independent Hamiltonians. To be able to observe the error behavior we increased the influence of the time dependent potential using a

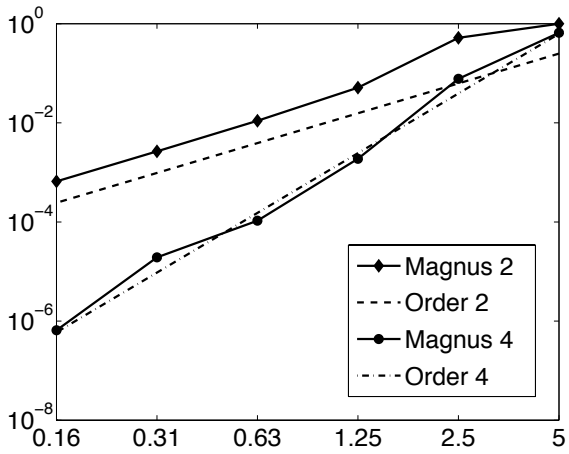

Figure 4: The error is plotted vs. time step size for the laser example with much larger laser frequency and amplitude. Magnus 2 (solid + diamonds) approximately matches the second order line (dashed), Magnus 4 (solid + circles) approximately matches the fourth order line (dash–dotted).

larger laser frequency of 2 instead of 0.0036 and an amplitude of 0.5513 instead of 0.0011.
In Fig. 4 we present the error on the wave function

$$\mathcal{E} = \|\psi_n^{ref} - \psi_n\|, \tag{48}$$

as a function of the time step, where ψ_n^{ref} is a reference solution. Both integrators show the expected error behavior.

5 Conclusions

Our group has considered time evolution methods for quantum systems. Due to the limited duration of the workshop we considered the simple one-dimensional problem given by the Hamiltonian in Eq. (4). Subgroups were formed to consider different integration schemes of second and fourth order and generally the expected convergence of the implementations was found. We have found that the Strang splitting, Crank-Nicolson, and second-order Magnus integration methods show quadratic convergence. Strang splitting scales better than Crank-Nicolson, since the FFT:s scale as $\mathcal{O}(N \log N)$, whereas the solution of the linear equation system of Crank-Nicolson scales as $\mathcal{O}(N^2)$. The fourth-order splitting and Magnus integration methods show fourth-order convergence. The splitting scheme scales as $\mathcal{O}(N \log N)$.

Due to the limited time we did not manage to consider any non-linear Hamiltonian in any detail. This would be the obvious continuation of the presented work since the majority of interesting problems in physics are non-linear. Such work would provide further experience about performance and scalability of the various methods considered. For non-linear problems the optimal convergence that we found for the linear problem is no longer expected and more thorough investigation of the various methods is needed to determine the optimal method for a given problem.

References

[1] S. Blanes and P. C. Moan. *Phys. Lett. A*, 265:35, 2000.

[2] A. Castro, M. A. L. Marques, and A. Rubio. *J. Chem. Phys.*, 121:3425, 2004.

[3] S. A. Chin. *Phys. Lett. A.*, 226:344, 1997.

[4] Marlis Hochbruck and Christian Lubich. On magnus integrators for the time-dependent schrödinger equations. *SIAM J. Numer. Anal.*, 41:945–963, 2003.

[5] C. Lanczos. An iteration method for the solution of the eigenvalue problem of linear differential and integral operators. *J. Res. Nat. Bureau Standards*, 45:255–281, 1950.

[6] Christian Lubich. *Quantum Simulations of Complex Many-Body Systems: From theory to Algorithms*, volume 10, chapter Integrators for Quantum Dynamics: A Numerical Analyst's Brief Review, pages 459–466. NIC Series, John von Neumann Institute for Computing, Jülich, Germany, 2002.

[7] W. Magnus. On the exponential solution of differential equations for a linear operator. *Comm. Pure Appl. Math.*, VII:649–673, 1954.

[8] M. A. L. Marques and E. K. U. Gross. *Annu. Rev. Phys. Chem.*, 55:427, 2004.

[9] R. I. McLachlan, G. Reinout, and W. Quispel. *Acta Numer.*, 11:341, 2002.

[10] C. B. Moler and C. F. Van Loan. Nineteen dubious ways to compute the exponential of a matrix. *SIAM Review*, 20:801–836, 1978.

[11] Y. Saad. Analysis of some krylov subspace approximations to the matrix exponential operator. *SIAM J. Numer. Anal.*, 29:209–228, 1992.

Group 2
Multiscale modeling of epitaxial growth

Mikko Byckling , Heikki Junes , Tommi Järvi ,
Sampsa Pursiainen , Axel Voigt

1 Introduction

This work concerns epitaxial growth, which is a modern technology of growing single crystals that inherit atomic structures from substrates. Modeling epitaxial growth is a challenging computational problem, since the growth process in macroscopic scale results from atomic processes in microscopic scale. The microscopic processes in epitaxial growth include the deposition of separate atoms or molecules on the terraces, adatom (adsorbed atom) desorption from and diffusion on the terraces as well as the attachment and detachment of adatoms to and from the steps.
For example, in the microprocessing industry, ability to grow thin films with good structure is of great importance. To precisely control the growth process requires a good knowledge of the atomic processes of the surface and the ability to simulate them. However, the simulation of the atomic processes is not usually able to reach time and length scales of interest for device applications.
On the surface of a grown crystal, atomic steps separate terraces that differ in height by a single lattice spacing. The movement of well-separated steps on a crystal close to equilibrium is classically described with the BCF model [1]. Typical unwanted growth behaviors which may show up in epitaxial growth are bunching and meandering of the terrace step edges, see Fig. 1. As one hopes to form a crystal which has as much regularity as possible, there is a need to simulate the terrace growth and the step movement as accurately as possible.
In this work, it is shown how a macroscopic continuum model of epitaxial growth can be constructed from the atomic processes. Both equilibrium and non-equilibrium models are discussed. The theory is formulated in terms of densities of adatoms ρ, kinks k and edge atoms φ that are defined to be those atoms which are bound to

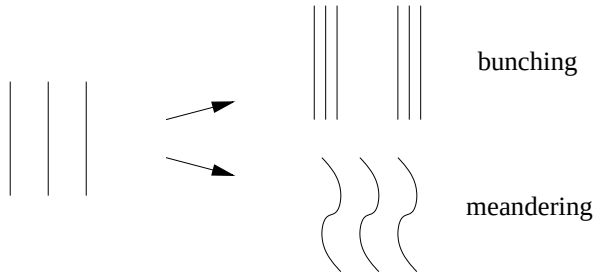

Figure 1: Bunching and meandering of steps.

a step edge but still move along the step. The dynamics of epitaxial growth at a microscopic level is specified in terms of diffusion coefficients. The macroscopic behavior of the growth process is modeled through a diffusion equation with boundary conditions which are derived directly from the microscopic processes.
Particular interest is paid on the following phenomenon: Experiments show that the attachment of an adatom to a step down is penalized compared to the attachment to a step up. In order to attach to a step from the upper terrace, an adatom must overcome an energy barrier known as the Ehrlich Schwoebel barrier. This phenomenon is studied by solving the adatom density numerically with different assumptions on the microscopic diffusion coefficients.
For a review on kinetic models in epitaxial growth see [2].

2 Terrace-step-kink model

2.1 Macroscopic fluxes

The adatom diffusion equation on a terrace i is

$$\partial_t \rho_i - D_T \nabla^2 \rho_i = -\tau^{-1} \rho_i + F_T - M_T \tag{49}$$

where ρ_i is the adatom density on terrace, and D_T is the adatom diffusion coefficient on a terrace, τ^{-1} is the desorption rate, F_T is the deposition flux rate onto the terrace, and M_T is the loss due to nucleation of adatom islands.
The velocity v_i of a step is determined by macroscopic fluxes of adatoms onto the step in the upper and lower terraces, $f_{i,+}$ and $f_{i,-}$. Their boundary conditions on the step are

$$-D_T \nabla \rho_i \cdot \vec{n}_i - v_i \rho_i = f_{i,+}, \tag{50}$$

$$D_T \nabla \rho_{i-1} \cdot \vec{n}_i + v_i \rho_{i-1} = f_{i,-}, \tag{51}$$

where $\vec{n}_i$ is the outer normal of the step. The adatom diffusion equation on an edge i is

$$\partial_t \varphi_i - D_E \partial_s^2 \varphi_i = F_{E,i} - M_{E,i}, \tag{52}$$

where φ_i is the adatom density on edge, and D_E is the adatom diffusion coefficient on an edge, $F_{E,i}$ is the net flux rate onto the edge, and $M_{T,i}$ is the loss of adatoms due to nucleation of kink pairs.
Kink density k on a step i evolves as

$$\partial_t k_i + \partial_s \left[w_i \left(k_{i,r} - k_{i,l} \right) \right] = 2 \left(g_i - h_i \right), \tag{53}$$

where w_i is the kink velocity, $k_{i,r}$ and $k_{i,l}$ are the right- and left-kink densities with $k_i = k_{i,r} + k_{i,l}$, g_i is the gain due to nucleation of kink pairs, and h is the loss due to annihilation of kinks.

2.2 Microscopic fluxes

Macroscopic fluxes are obtained from a kinetic model describing different microscopic processes between adatoms, step adatoms, and kinks. The macroscopic fluxes $f_\pm$ in Eq.s (50) and (51) are

$$f_\pm = (f_1^\pm + f_2^\pm + f_3^\pm + f_4^\pm) \cos(\theta), \tag{54}$$

where θ is the angle of the step with respect to [100] direction, and $f_j^\pm$ are the microscopic fluxes presented in Fig. 2. We derived these fluxes using the same prescription as in [3], but considering a greater density of adatoms on the terrace and on the edge.
To give an example of the construction of the fluxes, let us write the expressions for the two processes in Fig. 3. In the process on the left, a terrace adatom jumps to an edge adatom. Leaving out the index i and denoting the adatom density on the (upper) terrace below the line simply by ρ^+, the flux can be written as

$$a^2 \rho^+ (1 - ak)^2 D_{TE}^+ a^{-2} a^{-1} (1 - a\varphi), \tag{55}$$

where the factors, reading from the left and ignoring the lattice constant, are the probability to have an adatom on the terrace and to have no kinks on the edge, the diffusion constant of this process, and the probability to have no adatom on the edge already present. Similarly, the other process can be written as

$$a\varphi (1 - ak)^2 D_{ET}^+ a^{-2} a^{-1} (1 - a^2 \rho^+), \tag{56}$$

where the last factor is again the correction added in this work, and takes into account the possibility of already having an adatom on the terrace. These corrections are significant when the adatom densities are large, and hence may be required in non-equilibrium cases.

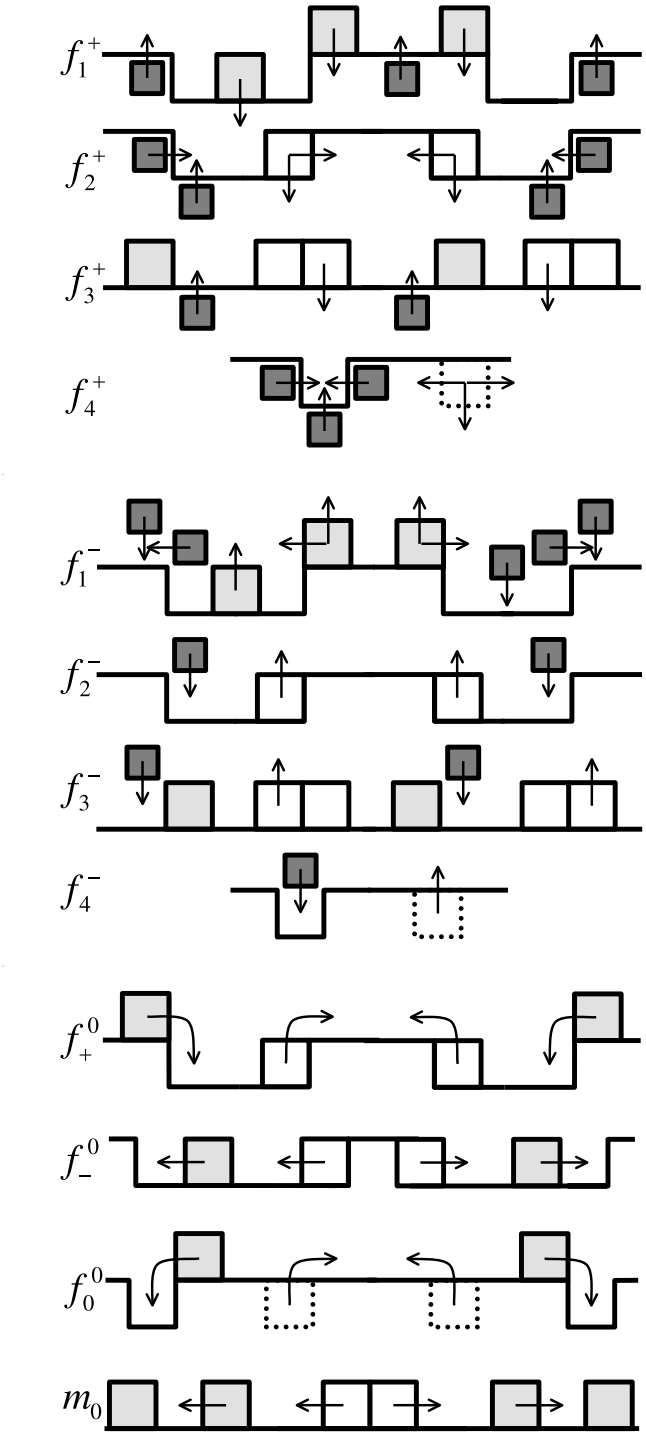

Figure 2: Microscopic processes contributing to the fluxes. The dark and light squares represent terrace and edge adatoms, respectively. The terrace drawn below the edge line is the higher one. Two adjacent adatoms form a pair of kinks of the edge.

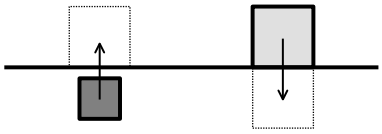

Figure 3: The simplest adatom diffusion processes between a terrace and an edge.

In conclusion, the corrections are embodied in the factors $(1-a^2\rho_i)$ and $(1-a\varphi_i)$, and they rescale the diffusion coefficients D_{XY} to the forms in square brackets below. The fluxes between the edge and the upper ('+') terrace are

$$\begin{aligned}
f_1^+ &= (1-ak_i)\left([D_{TE}^+(1-a\varphi_i)]a\rho_i - [D_{ET}^+(1-a^2\rho_i)]\varphi_i\right)a^{-2},\\
f_2^+ &= 2\,(1-ak_i)^2\,k_i\left(D_{TK}^+\rho_i - [D_{KT}^+(1-a^2\rho_i)]a^{-2}\right),\\
f_3^+ &= 2\,(1-ak_i)\left(D_{TK}^+a\,(1-ak_i)^2\rho_i\varphi_i - [(1-a\varphi_i)D_{KT}^+(1-a^2\rho_i)]k_{i,l}k_{i,r}\right)a^{-1},\\
f_4^+ &= 3\left(D_{TB}^+a\rho_i k_{i,l}k_{i,r} - [D_{BT}^+(1-a^2\rho_i)]\,(1-ak_i)^2\,a^{-3}\right),
\end{aligned}$$

where a is the lattice constant, and D_{XY}^+ are the diffusion coefficients that indicate hopping from X to Y, with X, Y indicating terrace (T), edge (E), kink (K), or bulk (B). Similarly, the fluxes between the edge and the lower ('-') terrace are

$$\begin{aligned}
f_1^- &= \left(1-a^2k_i^2\right)\left([D_{TE}^-(1-a\varphi_i)]a\rho_{i-1} - [D_{ET}^-(1-a^2\rho_{i-1})]\varphi_i\right)a^{-2},\\
f_2^- &= (1-ak_i)^2\,k_i\left(D_{TK}^-\rho_{i-1} - [D_{KT}^-(1-a^2\rho_{i-1})]a^{-2}\right),\\
f_3^- &= 2\,(1-ak_i)\left(D_{TK}^-a\,(1-ak_i)^2\rho_{i-1}\varphi_i - [(1-a\varphi_i)D_{KT}^-(1-a^2\rho_{i-1})]k_{i,l}k_{i,r}\right)a^{-1},\\
f_4^- &= D_{TB}^-a\rho_{i-1}k_{i,l}k_{i,r} - [D_{BT}^-(1-a^2\rho_{i-1})]\,(1-ak_i)^2\,a^{-3}.
\end{aligned}$$

And, the fluxes along the edge are

$$\begin{aligned}
f_+^0 &= (1-ak_i)^2\,k_i\left(D_{EK}^+a\varphi_i - [D_{KE}^+(1-a\varphi_i)]\right)a^{-2},\\
f_-^0 &= (1-ak_i)^3\,k_i\left(D_{EK}^-a\varphi_i - [D_{KE}^-(1-a\varphi_i)]\right)a^{-2},\\
f_0^0 &= 2\,(1-ak_i)\left(D_{EB}^+k_{i,l}k_{i,r}\varphi_i - [D_{BE}^+(1-a\varphi_i)]\,(1-ak_i)^2\,a^{-3}\right),\\
m^0 &= 4\,(1-ak_i)^2\left(D_{EK}^-\,(1-ak_i)^2\,\varphi_i^2 - [D_{KE}^-(1-a\varphi_i)^2]k_{i,l}k_{i,r}\right)a^{-1}.
\end{aligned}$$

In terms of the microscopic fluxes, the quantities $F_{E,i}$ and $M_{E,i}$ in Eq. (52) are

$$\begin{aligned} F_{E_i,i} &= \cos(\theta_i)(f_1^+ + f_1^- + f_+^0 + f_-^0 + f_0^0) \\ M_{E,i} &= \cos(\theta_i)(f_3^+ + f_3^- + m^0), \end{aligned}$$

and the quantities w_i, g_i, and h_i in Eq. (53) are

$$\begin{aligned} w_i &= \frac{a}{k_i}(f_+^0 + f_-^0 + f_2^+ + f_2^-), \\ g_i &= \frac{1}{2}m^0 + f_3^+ + f_3^-, \\ h_i &= f_4^+ + f_4^- + f_0^0. \end{aligned}$$

2.3 Equilibrium and detailed balance

To obtain the equilibrium values, we require the detailed balance condition. That is, all the microscopic fluxes separately vanish,

$$f_i^{\pm 1} = f_{0,\pm}^0 = m^0 = 0. \tag{57}$$

This results in equilibrium conditions,

$$\begin{aligned} \rho_i &= \left(\left[D_{ET}^{\pm}(1-a^2\rho_i)\right] / \left[D_{TE}^{\pm}(1-a\varphi_i)\right]\right)\varphi_i a^{-1} \\ \rho_i &= \left(\left[D_{KT}^{\pm}(1-a^2\rho_i)\right] / D_{TK}^{\pm}\right) a^{-2} \\ \rho_i &= \left(\left[(1-a\varphi_i)D_{KT}^{\pm}(1-a^2\rho_i)\right] / D_{TK}^{\pm}\right) k_{i,l}k_{i,r}/(1-ak_i)^2/\varphi_i a^{-1} \\ \rho_i &= \left(\left[D_{BT}^{\pm}(1-a^2\rho_i)\right] / D_{TB}^{\pm}\right) (1-ak_i)^2/(k_{i,l}k_{i,r})a^{-4} \\ \varphi_i &= \left(D_{KE}^{\pm} / \left[(D_{KE}^{\pm}) + D_{EK}^{\pm}\right]\right) a^{-1} \\ \varphi_i &= \left(\left[D_{BE}^{+}(1-a\varphi_i)\right] / D_{EB}^{+}\right) (1-ak_i)^2/(k_{i,l}k_{i,r})a^{-3} \\ \varphi_i^2 &= \left(\left[D_{KE}^{-}(1-a\varphi_i)^2\right] / D_{EK}^{-}\right) k_{i,l}k_{i,r}/(1-ak_i)^2, \end{aligned}$$

from which the second and fifth conditions yield the equilibrium adatom density on terraces, $\rho_i = \rho_{\rm eq}$, and on steps, $\varphi_i = \varphi_{\rm eq}$,

$$\begin{aligned} \rho_{\rm eq} &= \left(D_{KT}^{\pm}/D_{TK}^{\pm}\right) / \left[1 + (D_{KT}^{\pm}/D_{TK}^{\pm})\right] a^{-2} \\ \varphi_{\rm eq} &= \left(D_{KE}^{\pm} / \left[(D_{KE}^{\pm}) + D_{EK}^{\pm}\right]\right) a^{-1}, \end{aligned}$$

and fifth and seventh condition with $k_{i,l} = k_{i,r} = \frac{1}{2}k_i$ yield the equilibrium density of kinks, $k_i = k_{\rm eq}$,

$$k_{\rm eq} = \frac{1}{a}\left(1 + \frac{\sqrt{D_{EK}^{\pm}/D_{KE}^{\pm}}}{2}\right)^{-1}, \tag{58}$$

which is in agreement with BCF theory [1] for the case when the height of kinks is limited to ± 1.

3 Planar steady-state solution

In this section, it is shown how the microscopic fluxes can be used to derive a planar quasi-steady-state solution. In the following computations, it is assumed that the crystal surface consists of a periodic sequence of steps which are separated by distance L that move at velocity v towards the normal direction of the step edges ([010] direction).
By making a quasi-steady state approximation, neglecting nucleation of the two-dimensional islands on terraces as well as desorption and applying the requirements for detailed balance, the diffusion equation becomes

$$-D_T \nabla^2 \rho = F. \tag{59}$$

The solution is the adatom density ρ, which is given by

$$\rho(x,t) = -\frac{F}{2D_T}\Big((x-vt)^2 - L^2\Big) + C_1(x-vt) + C_2 \tag{60}$$

where $C_1 = (\rho_+ - \rho_-)/2$ and $C_2 = (\rho_+\rho_-)/2$ are unknown coefficients. The densities ρ_+ and ρ_- are the adatom densities on the terrace edges. Coefficients C_1 and C_2 can be solved from the boundary conditions

$$\mathbf{\Psi}(k,\varphi,\rho_+,\rho_-) = \begin{pmatrix} D_T C_1 - FL + f_+ \\ D_T C_1 + FL - f_- \\ f_1^+ + f_1^- - f_0 - m \\ g - h \end{pmatrix} = \mathbf{0}, \tag{61}$$

where $f_j^{\pm}$ are the microscopic fluxes, $m = (m^0 + f_3^+ + f_3^-)\cos(\theta)$, $g = m_0/2 + f_3^+ + f_3^-$, $h = f_0^+ + f_4^- + f_0^0$ and $f_0 = (f_+^0 + f_-^0 + f_0^0)\cos(\theta)$. This is a non-linear system of equations that can be solved numerically by using the Newton's method

$$\mathbf{x}^{i+1} = \mathbf{x}^i - \nabla\mathbf{\Psi}(\mathbf{x}^i)^{-1}\mathbf{\Psi}(\mathbf{x}^i), \tag{62}$$

where $\nabla\mathbf{\Psi}(\mathbf{x}^i)^{-1}$ is the inverse of the Jacobian matrix of $\mathbf{\Psi}$ evaluated at the point $\mathbf{x}^i = (k^i, \varphi^i, \rho_+^i, \rho_-^i)$.

3.1 Results

The system is solved numerically with $F = 0.1$, $L = 1000$, $D_E = 1 \cdot 10^5$, $D_T = 1 \cdot 10^{12}$ and $\theta = 0$, which corresponds to the condition that the terrace edges are parallel and perpendicular to the direction of propagation [010]. The terraces are assumed to be ordered so that lower terrace levels are found as x in Eq. (60) increases. The diffusion constants are chosen as

$$\begin{aligned} D_{XY}^- &= D_X \\ D_{XY}^+ &= (1-\beta)D_X \end{aligned}$$

for $XY = \{ET, TE, TK, KT, TB, BT\}$ and $D^{\pm}_{XY} = D_X$ for $XY = \{EB, BE, EK, KE\}$. The parameter $\beta \in [0, 1]$ defines the bias between the diffusion constants and by varying it one can control the level of Ehrilch Schwoebel effects. Three values $\beta = \{0, 0.99, 1\}$ were tested in the calculation of the steady-state distribution.

The solution in Fig. 4 was computed by applying Newton iteration in Eq. (62). Figure 5 shows the convergence behavior of the method.

4 Conclusions

The modified microscopic fluxes make the terrace-edge-kink model more useful in far-from-equilibrium situations. In a high density of adatoms on the terraces and edges, one has to take into account, for example, whether there is already an adatom on the terrace to which an adatom diffuses from the edge. As a result, the diffusions rates between the terrace, edge, and kinks slightly rescale into smaller values.

In the detailed balance of the microscopic fluxes, the equilibrium density of adatoms on terrace, ρ_{eq}, edge, φ_{eq}, and kinks, k_{eq}, were calculated. The correction which was made to the microscopic fluxes decreased ρ_{eq} and φ_{eq}, but retained k_{eq} the same.

The numerical experiments yield qualitatively three different kind of steady-state solutions. When β is chosen to be zero the solution curve tilts towards the right terrace edge so that there is a positive flux of adatoms to the next (lower) terrace but the flux to the previous (upper) terrace is close to zero. This condition causes typically bunching of the terraces.

In the second case, where $\beta = 0.99$, the fluxes to both directions are close in magnitude. Since the differences are clearly smaller than in the first case, this condition will cause a more stable structure of the terraces.

When $\beta = 1$ there is a flux to the negative direction, which will easily cause meandering of the terraces. Meandering is constant variation of the terrace edges in shape and distance.

In industrial applications, one usually wants to make the growth of the lattice stable. Therefore bunching and meandering are often classified as unwanted phenomena. Within this interpretation the choice $\beta = 0.99$ is close to the optimal value for the bias parameter. However, it is difficult to control the growth parameters with present techniques. One way to possibly control the bias in diffusion is to grow the crystal in an electrical field.

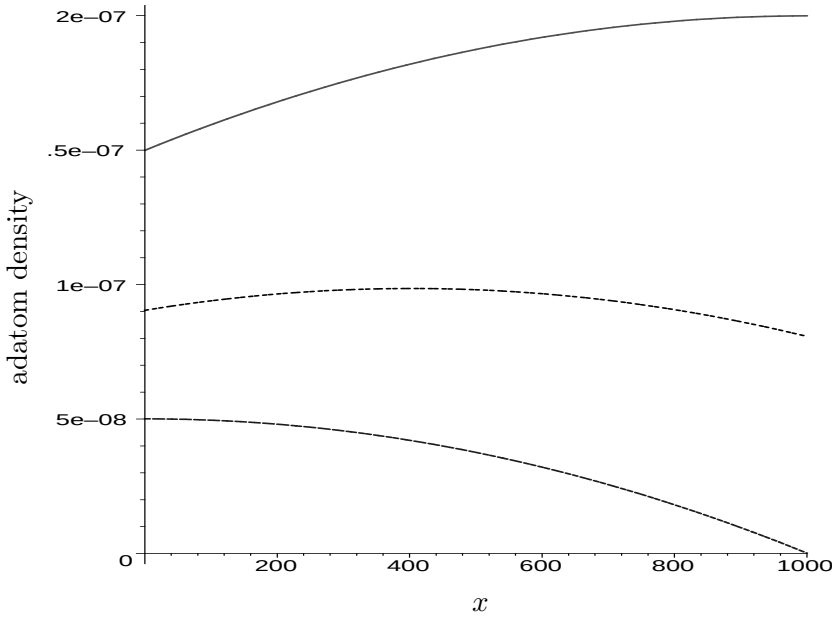

Figure 4: Planar steady-state adatom density on a terrace between $x = 0 \ldots 1000$. Lines: top (solid) $\beta = 1$, middle (dash-dotted) $\beta = 0.99$, bottom (dashed) $\beta = 0$.

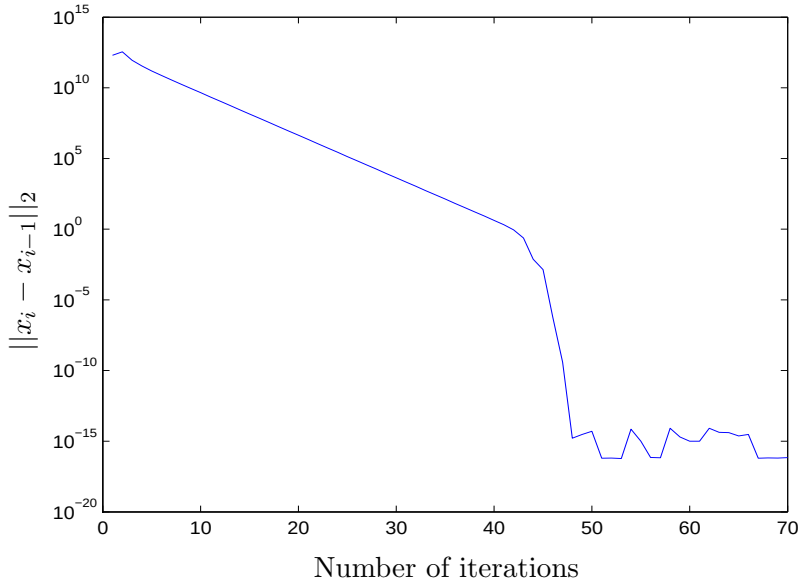

Figure 5: Convergence of the Newton iteration for $\beta = 0$

References

[1] W. K. Burton, N. Cabrera, F. C. Frank, Phil Trans. Roy. Soc. London Ser. A **243**, 299 (1951).

[2] R. E. Caflisch, Weinan E, M. F. Gyure, B. Merriman, and C. Ratsch, Phys. Rev. E **59**, 6879 (1999).

[3] L. Balykov and A. Voigt, to appear in Phys. Rev. E (2005).

Group 3
Markov Chains and Monte Carlo Simulations Without Detailed Balance

Students: Simo Ali-Löytty, Christian Flindt, Anders Hansson, Mika Jahma, Mads Jensen, Laura Koponen, and Erik von Schwerin

1 Introduction

A Markov chain is a stochastic process with no memory, that is, the probability of the system being in a state depends only on the probability of being in a previous state. The Monte Carlo (MC) simulation method is based on the theory of stochastic Markov chains. In a MC simulation, the configuration of the system of interest is changed by a series of random moves. The moves form a Markov chain such that a desired probability distribution is achieved. Since its introduction in 1953 [1] the Markov chain Monte Carlo method has been widely used in versatile applications, especially in estimating average properties of many-body systems with a very large number of accessible states with either discrete or continuous degrees of freedom. Let us consider a system with discrete and finite number of states $\{i\}$. Let us assume that the system is in a canonical ensemble. That means that the limiting distribution of the Markov chain is the Boltzmann distribution

$$p_i^* = \exp -\beta E_i/Z, \tag{63}$$

where E_i is the energy of the state i, Z is the partition function (normalization) and $\beta = 1/k_B T$ is the inverse temperature of the system.
Let the vector p^* denote the desired equilibrium probability distribution of the states, satisfying $Pp^* = p^*$. The matrix P is the transition matrix. Its entries P_{ij} are the transition probabilities from the state i to the state j.

The temporal evolution of a Markov chain starting from some initial state p_0 is governed by the Master equation

$$\frac{\partial p_i}{\partial t} = -\sum_{j=1}^{N}[w_{ij}p_i - w_{ji}p_j], \tag{64}$$

where $w_{ij} = P_{ij}/\tau$ are the transition rates. For simplicity, we assume the arbitrary transition time to be scaled to $\tau = 1$. By setting each term in Eq. (64) individually to zero we get the usual detailed balance condition (DBC)

$$P_{ij}p_i^* = P_{ji}p_j^* \tag{65}$$

If the DBC is enforced, it is easy to use it to construct any desired probability distribution. One such simple scheme is the Metropolis MC simulation. The algorithm reads:

0. Start from an initial configuration $i(0)$

1. Move by random δ: $\tilde{i} = i(t = k) + \delta$

2. Accept the move with probability $\min(1, p(\tilde{i})/p(i(k)))$

3. If accepted, $i(k + 1) = \tilde{i}$; if not, $i(k + 1) = i(k)$

4. Return to 1.

The DBC is obviously a sufficient but not necessary condition in a MC simulation, because there is no fundamental reason why each transition should pairwise satisfy Eq. (65). In fact, there are many MC methods in wide use that do not satisfy the DBC, such as the sequential updating of spins in the Ising method.

2 Monte Carlo simulations without detailed balance

As stated above, it is clear that the detailed balance is only a sufficient condition, not necessary, and as shown by Manousioutakis and Deem the detailed balance is an overly strict condition to ensure a valid Monte Carlo simulation [2]. This observation has been exploited by several authors in order to develop more efficient Monte Carlo algorithms.

2.1 Proposal for speed-up

In the following we consider a recent proposal put forward by Frenkel for speeding up Monte Carlo simulations by sampling of rejected states [3]. The Metropolis algorithm is based on the generation of trial moves from the current state (i) to a new state (j), *e.g.* the flip of a spin on a single site leading to a new Ising configuration. Imposing the detailed balance condition as expressed in Eq. (65), the probability for accepting the new state can be chosen as [1]

$$P_{ji} = \min\left\{1, \frac{p_j^{\text{stat}}}{p_i^{\text{stat}}}\right\}. \tag{66}$$

The detailed balance condition ensures that each state is visited with a frequency corresponding to the desired distribution contained in p^*, *e.g.* the Boltzmann distribution for classical systems in thermal equilibrium. Consequently, at the end of the simulation the expectation value of interest $\langle A\rangle$ can be approximated by an *unweighted* average over visited states, *i.e.*

$$\langle A\rangle \simeq \frac{\sum_i N_i A_i}{\sum_i N_i}. \tag{67}$$

Here A_i is the value of the stochastic variable A in the state i, and N_i is the number of times that the state i was visited during the simulation. The sum runs over all states visited during the simulation. The total number of visits $N = \sum_i N_i$ should be chosen such that the approximation to $\langle A\rangle$ expressed in Eq. (67) does not vary significantly with a further increase of N.

The proposal by Frenkel takes into account the states that are rejected in standard Markov chain Monte Carlo (MCMC) schemes, *e.g.* the aforementioned Metropolis algorithm, and thus are not visited. Frenkel argues that "this approach leads to a dramatic improvement in the statistical accuracy of Monte Carlo simulations" [3]. We start by reviewing the proposal, taking its application to the Metropolis algorithm as an example. The method, however, is applicable to any valid MCMC scheme [3].

The algorithm proposed by Frenkel adds an extra element to the Metropolis algorithm. In each Monte Carlo step i, *i.e.* each step during which a trial step (or set of trial sets in other MCMC schemes) is proposed and possibly accepted, the *weighted* average

$$S_i = \frac{w_1 A_1 + w_2 A_2}{w_1 + w_2} \tag{68}$$

is formed. Here $1, 2$ denote the two possible final states, which are the original state (in case the trial state was rejected) and the trial state. The weights $w_{1,2}$ are given

[1] Another possible choice is $P_{ji} = \frac{1}{1+p_i^{\text{stat}}/p_j^{\text{stat}}}$, which also obeys the detailed balance condition.

by the probability of being in the corresponding state according to p^*, *e.g.* the Boltzmann distribution. After the final state has been determined, the algorithm proceeds with the next Monte Carlo step as described above, and finally, after the desired number M of Monte Carlo steps have been carried out, the expectation value of interest $\langle A \rangle$ is estimated as

$$\langle A \rangle \simeq \frac{\sum_{i=1}^{M} S_i}{M}, \tag{69}$$

where M is chosen such that the estimate to $\langle A \rangle$ does not vary significantly with increasing M.

The proposal by Frenkel can be shown to satisfy the balance condition [3] (not to be confused with the *detailed* balance condition). As expressed in Ref. [2], the balance condition requires that the desired distribution, *e.g.* the Boltzmann distribution, is left invariant by the Markov chain mimicking the Monte Carlo simulation. Moreover, the proposal can be shown to obey so-called *superdetailed balance* [3], which despite of the name is a weaker condition than the detailed balance condition. The superdetailed balance fulfills the conditions given by Manousioutakis and Deem [2], and is thus sufficient to ensure the validity of Frenkel's proposal [3]. We shall refrain at this point from discussing superdetailed balance in further detail. We refer the interested reader to the work by Frenkel for a thorough discussion of superdetailed balance [3].

2.2 Implementation and results

In order to test the proposal by Frenkel, we implemented the Metropolis algorithm with the additional steps as described above. The results showed – *numerically* – that the algorithm proposed by Frenkel leads to the same results as the standard Metropolis algorithm. However, no increase in computational efficiency was observed. This is in accordance with Frenkel who states [3] that the advantages of his proposal are limited when applied to e.g. conventional MCMC simulations with a simple spin flip dynamics. To obtain an increase in computational efficiency the method should be applied in cases where a very large number of trial states are generated in parallel [3]. This is naturally done in the cluster algorithms such as Wolff or Swendsen–Wang algorithms for flipping clusters of spins at one step instead of one spin.

In order to test this statement, we applied the proposal by Frenkel to a Swendsen–Wang (SW) cluster algorithm [4] for the nearest neighbor Ising model. The algorithm is implemented as follows. A cluster of spins is constructed such that if two neighboring spins have the same orientation, they belong to the same cluster with the probability $1 - \exp(-K)$, where $K = J/(k_B T)$, and J is the coupling

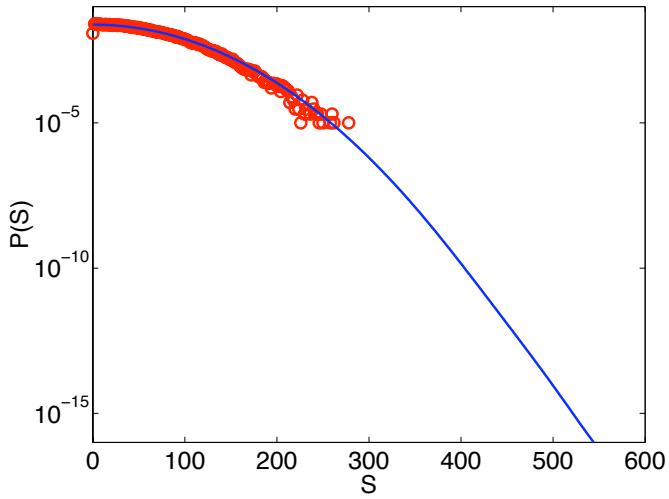

Figure 1: The histograms for the total spin in the 32×32 lattice are shown for the Frenkel's method (solid line) and conventional Swendsen–Wang implementation (open circles). As can be seen, the Frenkel's method gives more accurate results and spans a wider range in the spin values. The scatter in the data indicates the errors.

constant of the Ising Hamiltonian. The clusters in the lattice are then flipped with probability 1/2. In constructing the clusters with one lattice sweep we have used the Hoshen-Kopelman algorithm [5]. In the simulations the lattice size was 32×32, $K = 0.30$, and 50 000 updates after equilibrating over 10 000 steps. It must be noted that with SW algorithm once the spin clusters have been chosen, the probability of obtaining any possible final value for the total spin is uniform. Thus, once we have constructed the clusters, each cluster is flipped independently of the others.

In equilibrium we sample in principle all possible values of the total spin. In Fig. 1 we show this distribution of the total spin obtained with the Frenkel's method (solid line) and the ordinary SW (open circles). As stated in Ref. [3] the new method clearly outperforms the typical sampling in accuracy and also spans a wider range of the total spin values. This is expected since the new method utilizes all cluster configurations generated with one lattice sweep when calculating the estimates for the average quantities.

3 Transition matrix approach

Next we consider approach the problem of violating the strict detailed balance condition from a slightly different point of view. In the following we wish to investigate the convergence rate of a MC simulation based upon knowledge of the eigenvalues of the corresponding transition matrix of the Markov chain.
Consider a physical system which is described by a finite number of states r_i (configurations) with probability of states p_i. As discussed above, if the physical process evolving this system is described by a stochastic process with no memory the evolution process is described by a Markov chain,

$$p_i = A(p_{i-1}) \text{ or in matrix notation } \boldsymbol{p}_i = \mathrm{A}\boldsymbol{p}_{i-1}, \tag{70}$$

where A is the transition matrix. In general in physical systems of interest the transition matrix A is extremely large. It is thus very inconvenient to evolve the system according to Eq. (70), in stead the probability of states are evolved by the Monte Carlo (MC) simulation method. In a MC simulation only the probability of states vector $\boldsymbol{p}$ and the states vector $\boldsymbol{r}$ are stored in memory. The evolution of the system is now governed by having knowledge of the hamiltonian of the system and by means of a random "flip between states" model. The hamiltonian may, e.g., be of type long range or nearest neighbor. The flip model may be, e.g., of type single flip, random total flip, or cluster flip (Wolff).

3.1 Problem: mathematical formulation

Our problem is to find the optimal transition matrix A, which fulfills the following conditions

- $\mathrm{A}_{ij} \geq 0, \quad \forall i, j$
- $\sum_i \mathrm{A}_{ij} = 1, \quad \forall j$
- $\mathrm{A}\mathbf{p} = \mathbf{p}$,

where $\mathbf{p} \in \mathbb{R}^n$ is the steady state distribution. By optimal we mean that the convergence of

$$\lim_{M\to\infty} \mathrm{A}^M \mathbf{p}_{arb.} = \mathbf{p} \tag{71}$$

is as fast as possible, where $\boldsymbol{p}_{arb}$ is an arbitrary initial condition. The convergence rate of the process described in Eq. (71) is given by

$$\|\mathrm{A}^M \mathbf{p}_{arb.} - \mathbf{p}\| \leq C|\lambda_2|^M, \tag{72}$$

where $|\lambda_2|$ is the second largest eigenvalue of A. So one way to increase convergence speed is to minimize $|\lambda_2|$. The convergence of the system Eq. (71) is guaranteed if we enforce detailed balance (see other chapters).
If we know the steady state solution $\mathbf{p}$ then the optimal transition matrix is $\mathrm{A} = \mathbf{p}\mathbf{1}^T$, where $\mathbf{1}$ is a vector with every element is one. Unfortunately the dimension of the steady state distribution is in general so large (e.g., $n = 2^{1000}$ with 1000 "spins" or particles) that we do not have computational power to calculate it. Because of this we find a transition rate function

$$f: \ \mathrm{A}_{ij} = f\left(\frac{\mathbf{p}_j}{\mathbf{p}_i}\right), \tag{73}$$

so that the number of nonzero elements N of A is small and $|\lambda_2|$ is small. Understandably we thus try to find a transition matrix so that the computational time is as small as possible. This criterion is roughly the same as requiring fast convergence of

$$\lim_{MN\to\infty} \mathrm{A}^M \mathbf{p}_{arb.} = \mathbf{p}. \tag{74}$$

In the following sections we investigate the behavior of the convergence speed, the size of the eigenvalue $|\lambda_2|$, and of the error. We do that by comparing different types of the transition rates (Metropolis and Kawasaki), different types of update schemes (single flip and random configuration flip), and different types of hamiltonians (long range and nearest neighbor). Also note that we do not fiddle with the detailed balance condition to perform this study. The different MC models where implemented in MatLab.

3.2 Small example: Randomly flip only one spin

As a first example assume that we have a system of nine spin then the number of states is $n = 2^9 = 512$ (either spin up or spin down). In the MC simulation we randomly flip one spin and the hamiltonian only includes nearest neighbor interactions. In Fig. 2 we compare the Metropolis and Kawasaki models. The error is calculate by following

$$\mathrm{Error}(M) = \sum_{i,j} |\left[\mathrm{A}^M - \mathbf{p}\mathbf{1}^T\right]_{ij}|. \tag{75}$$

For this first small example the chosen parameters make the Metropolis model converge the fasts.
Table. 3 includes values for the second largest eigenvalues and converges rates. We notice that the second largest eigenvalue gives a quite accurate limit for the convergence exponents.

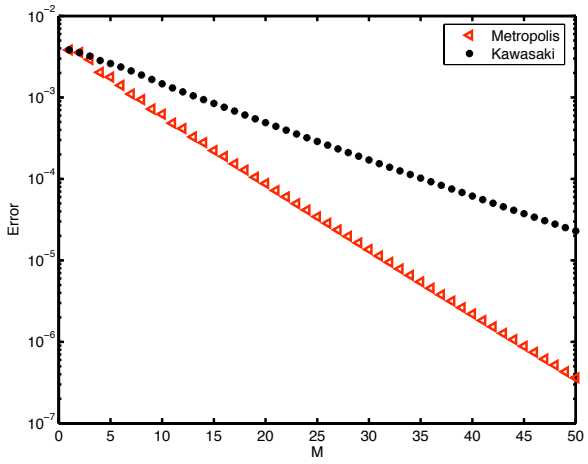

Figure 2: Temperature is $k_bT = 1$, nearest neighbor hamiltonian

	$\lvert\lambda_2\rvert$	$10^{''slope''}$
Metropolis	0.84	0.83
Kawasaki	0.91	0.90

Table 3: Convergence rates: analytic and simulated corresponding to the results shown in Fig. 2.

3.3 Convergence dependency

In Figs. 3 and 4 we have calculated the second largest eigenvalue $|\lambda_2|$, they are depicted as function of the energy k_bT. The energy k_bT enters the transition rate function f in Eq. (73). As mentioned we compare the Metropolis and the Kawasaki models having,

$$f_{\text{Metro}} = \begin{cases} \exp(-\delta E/k_bT) & \text{if } \delta E > 0 \\ 1 & \text{if } \delta E \leq 0 \end{cases} \tag{76}$$

$$f_{\text{Kawa}} = \frac{1}{2}\left[1 - \tanh(\delta E/k_bT)\right], \tag{77}$$

where δE is the difference in energy between two states r_i and r_j. We have used the Boltzmann statistics so that $\frac{\mathbf{p}_j}{\mathbf{p}_i} = \exp(-\delta E/k_bT)$, so f_{Metro} and f_{Kawa} can be written as in the form of Eq. (77). For the following simulations we have chosen a system consisting of $n = 9$ spins and we perform $M = 10000$ iterations in the MC simulation.

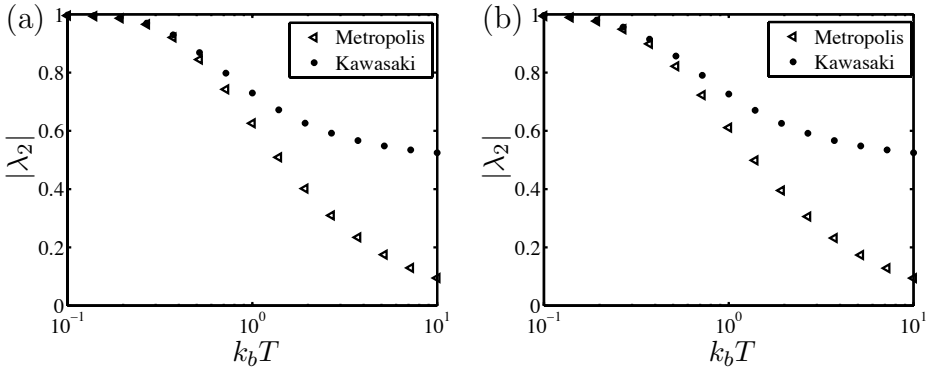

Figure 3: (a) Long range weak interaction, flipping to a random new state r_i ,and (b) Short range interaction, flipping to a random new state r_i.

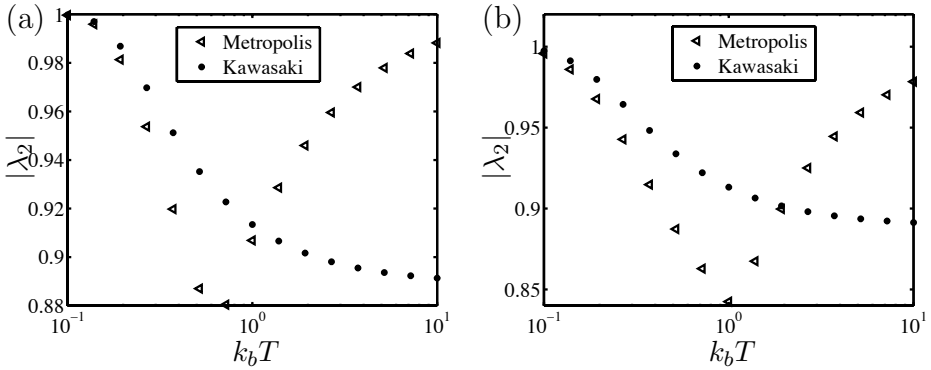

Figure 4: (a) Long range weak interaction, flip only single random spin in the configuration r_i, and (b) short range interaction, changing only single random spin in the configuration r_i.

From the figures it is evident that there is a clear dependence on of the eigenvalue $|\lambda_2|$ on the energy k_bT as well as on the hamiltonian and the updating scheme. Note that for the long and short range interactions the difference are not very large, but noticeable. Because of the size of the system ($n = 9$) all sites are sort of "neighbors".

4 Conclusions

In conclusion we have reviewed and discussed the possibility of constructing Monte Carlo simulation schemes that do not obey the detailed balance condition. In particular, we have studied a recent proposal for speeding up Monte Carlo simulations by extending existing proposals, taking into account rejected trial states. The proposed algorithm obeys the so-called superdetailed balance condition, which is sufficient to ensure a valid Monte Carlo simulations, however without being as strict as the detailed balance condition. We have applied the method to two existing Monte Carlo algorithms, the Metropolis algorithm and the Cluster algorithm, and found that the method in case of the Cluster algorithm provides an increase in computational efficiency compared to the original algorithm. By examining the second largest eigenvalue of the transfer matrix we also investigated the speed of convergence of Metropolis and Kawasaki updating schemes. We found that there are differences in the convergence between short and long range interactions as well as between the updating schemes. We see that depending on the physical system studied and the temperature the choice for the specifics of the MC simulations are important when concerned with convergence speed.

References

[1] N. Metropolis, A. Rosenbluth, M. Rosenbluth, A. Teller, and E. Teller, *J. Chem. Phys.* **21**, 1087 (1953).

[2] V.I. Manousioutakis, M.W. Deem, *J. Chem. Phys.* **110**, 2753 (1999).

[3] D. Frenkel, *PNAS* **101**, 17571 (2004).

[4] R.H. Swendsen and J.S. Wang, *Phys. Rev. Lett.* **58**, 86 (1987).

[5] J. Hoshen and R. Kopelman, *Phys. Rev. B* **1**, 3438 (1976).

Group 4
Electrohydrodynamic stability analysis of two-phase flows in confining microsystems

C. V. Achim, T. Ambjörnsson, J. Ö. Bakke,
K. Krupchyk, E. Kuusela, T. Laurila,
M. Lomholt, A. Loubenets, O. Punkkinen,
W. Villanueva, G. Goranović and H. Bruus

1 Introduction and description of the system

(Presented by Teemu Laurila)
We are considering flow of two immiscible liquids in a wide and shallow microchannel, i.e., essentially between two parallel planes, Fig. 1. The flow is a steady-state Couette-Pouiseuille flow driven by an upper moving wall, and the interface between the two liquids is exposed to an electric field either normal or parallel to the flow. The problem was to investigate the conditions of instability of the interface in the small Reynolds number regime as well as with respect to the values of normal and tangential fields.
Assuming incompressible flow, the Navier-Stokes equations governing the 2D flow (U, W), are simplified to

$$RD_tU = -\partial_x P + \nabla^2 U \tag{78}$$
$$RD_tW = -\partial_z P + \nabla^2 W \tag{79}$$
$$\partial_x U + \partial_z W = 0, \tag{80}$$

for both liquid domains separately. The boundary conditions at the walls are no-slip. At the interface we have continuity of flows, no tangential stress, and the surface tension balances the normal stress.
Assuming the liquids are perfect dielectrics, the electric potential obeys the Laplace equation

$$\nabla^2 \Phi = 0. \tag{81}$$

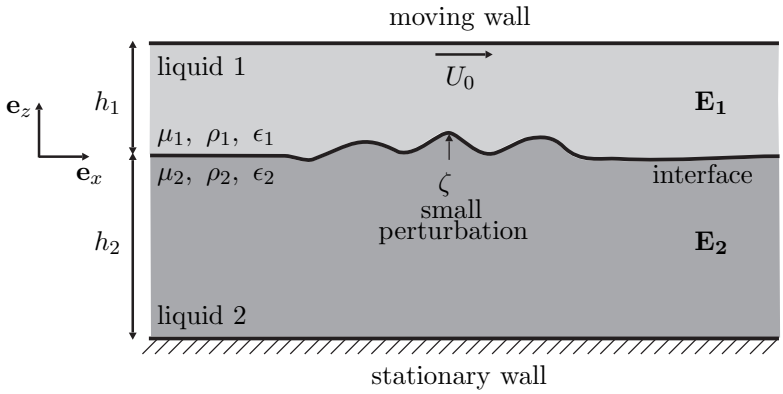

Figure 1: Two streaming fluid dielectrics confined between two infinite, microscopically spaced plates. The liquids differ in mass density, viscosity and dielectric constants, and occupy different depths of the microchannel. The liquids are in addition exposed to an electric field. U_0 is a slip (driving) velocity at the wall.

The boundary conditions are given by a potential difference between the cathodes. At the interface we have the continuity of tangential electric fields, and the normal electric field changes as given by the difference between dielectric constants. Coupling between fluid and electric equations comes only by the stress the electric field introduces at the interface.

2 Perturbed flow: governing equations and boundary conditions

(Presented by Teemu Laurila and Alexei Loubenets) We are looking into the stability of a small perturbation in the interface

$$\zeta(x,t) = \zeta_0 e^{ik(x-ct)}. \tag{82}$$

where $c = \text{Re } c + i\text{Im } c$ is the complex phase velocity. The perturbations are unstable if $\text{Im } c > 0$.
The dispersion relation $c(k)$ for our system is obtained by linearizing in $\zeta(x,t)$. This linearization for all the fields $F \in \{U, W, P, \Phi\}$ is obtained by expanding explicitly in ζ, and in fluctuations $F^{(1)}$ *implicitly* caused by ζ

$$F(\zeta) = F^{(0)}(0) + \zeta \partial_z F^{(0)}(z)|_{z=0} + F^{(1)}(0) + ... \tag{83}$$

This expansion in a *function* ζ, can be formally written with a "counter" α

$$F(\zeta) = F^{(0)}(0) + \alpha[\zeta \partial_z F^{(0)}(z)|_{z=0} + F^{(1)}(0)]$$
$$+\alpha^2[\frac{1}{2}\partial_z^2 F^{(0)}(z)|_{z=0} + 2\zeta \partial_z f^{(1)}(z)|_{z=0} + F^{(2)}(0)] + ...$$

Linearization in this way produces a system of equations that depend on the fluctuations $U^{(1)}$,$W^{(1)}$,$P^{(1)}$,$\Phi^{(1)}$, *as well as* $\zeta(x,t)$. By solving this (linear) system of equations for the fluctuations $F^{(1)}(x,z,t) = f^{(1)}(z)e^{ik(x-ct)}$ we obtain the dispersion relation.
In the linearized equations, the flow is a potential flow given by

$$(U,W) = (\partial_z\Psi, -\partial_x\Psi), \tag{84}$$

where the flow potential is also of form $\Psi^{(1)}(x,z,t) = \psi^{(1)}(z)e^{ik(x-ct)}$. The linearized system of equations then reduces to one ordinary differential equation for ψ. It is the Orr-Sommerfeld equation, which at 4^{th} order is rather complicated

$$\psi_j^4 - 2k^2\psi_j^2 + k^4\psi_j = ikRe_j\left((u_j^0 - c)(\psi_j^2 - k^2\psi_j) - u_j^0\psi_j\right) \qquad \text{for} \quad j = 1,2 \tag{85}$$

where ψ_1, ψ_2 are the stream functions for the upper and lower liquids, k is the wave number, Re is the Reynolds number and c is the complex phase velocity of the displacement ζ defined in Eq. 82.
Additionally, we have no slip boundary conditions at rigid boundaries

$$\psi_2(-n) = \psi_2'(-n) = \psi_1(1) = \psi_1'(1) = 0 \tag{86}$$

and four jump conditions between ψ_2 and ψ_1 at the interface point ($z = 0$)

$$\begin{aligned}
\psi_1(0) &= \psi_2(0) && (87)\\
\psi_1'(0) - \psi_2'(0) &= \frac{\psi_1(0)}{c-b}(1-m)a_2 && (88)\\
\psi_1''(0) + k^2\psi_1(0) &= m(\psi_2''(0) + k^2\psi_2(0)) && (89)\\
m(\psi_2'''(0) - 3k^2\psi_2'(0)) &+ irkRe_1((c-b)\psi_2'(0) + a_2\psi_2(0))\\
-(\psi_1'''(0) - 3k^2\psi_1'(0)) &+ irkRe_1((c-b)\psi_1'(0) + a_1\psi_1(0))\\
= ik(k^2S &+ T_{el})\frac{\psi_1(0)}{(c-b)} && (90)
\end{aligned}$$

where a_1, a_2, m , S and T_{el} are some given quantities. Note, that we are interested in finding both c and the stream functions ψ. The phase velocity c will give us the required value of the perturbation ζ (via Eq. (82)). At the same time, with help of c and the stream functions ψ_1, ψ_2 we will be able to reconstruct the first-order flow field through Eq. (84) and

$$\left(\Psi_j, P_j^{(1)}\right) = \left(\psi_j(z), p_j^{(1)}(z)\right)\exp\left(ik(x-ct)\right) \qquad \text{for} \quad j = 1,2 \tag{91}$$

The Orr-Sommerfeld Eq. (85) together with the boundary conditions, Eqs. (86) - (90), can be solved numerically, or additionally expanded in terms of small Reynolds number (characteristic for microsystems), i.e., limit $R \to 0$, and analytically solved for different orders of expansion, yielding a dispersion relation.
Our work proceeded from this point in three directions. We tried both, the numerical solution of the Orr-Sommerfeld equation and the BCs with non-zero Reynolds number, and the zero-order analytic expression of the dispersion relation in the expansion for very small Reynolds number. Finally we also simulated the original hydrodynamics problem using a fluid dynamics solver, that included a diffuse interface between the two immiscible liquids.

3 Numerical solution: determining the phase velocity and the stream function

(Presented by Alexei Loubenets) We decided to split the initial task (that is to obtain both phase velocity and stream functions) in two parts:

1. Fix the value of c (some initial guess, based on zero-order approximation)
2. With the fixed c solve Orr-Sommerfeld equations for ψ_1 and ψ_2
3. Using ψ_1 and ψ_2 update the guess for c and repeat all steps until some relative tolerance is met.

In step (**2**) we decided to apply *Shooting* method, namely to solve the given boundary value problem as an initial value problem. Thus we proceed as follows

1. Make an initial guess of $\psi_1''(1)$ and $\psi_1'''(1)$
2. Define $Y_1 = [\psi_1, \psi_1', \psi_1'', \psi_1''']$ and solve the initial value problem for the upper liquid
$$\begin{cases} Y_1' = F_1(z, Y_1) \\ Y_1(1) = g_1 \end{cases}$$
for $z \in [1, 0]$
3. Define $Y_2 = [\psi_2, \psi_2', \psi_2'', \psi_2''']$ and use the jump relation at the interface point $z = 0$ to obtain the initial guess $Y_2(0) = g_2$
4. Solve the IVP for the lower liquid
$$\begin{cases} Y_2' = F_2(z, Y_2) \\ Y_2(0) = g_2 \end{cases}$$
for $z \in [0, -n]$

5. Use Newton method to update the initial guess $\psi_1''(1)$ and $\psi_1'''(1)$

Unfortunately, this approach (fixing c and solving Orr-Sommerfeld equations for ψ_1 and ψ_2 only) turned to be unfitted for our problem. It is only the trivial solution that we were able to capture. Thus, for this problem, we suggest to use some more establish techniques such as: *Compound Matrix method* or *FEM* type method.

4 Analytic solution: zero order dispersion relation c(k)

(Presented by Jan Öystein Bakke)
The zero-order dispersion relation was taken from equation (102 b) of Ref. [1].
The Figs. 2-4 show Im $c^{[0]}$, i.e., the imaginary part of the phase velocity of a plane wave perturbation of the solution of the Orr - Sommerfeld's equations to the zeroth-order in small Reynolds number, described in the paper referred to above. We observe that there exist unstable long wavelengths perturbations, and that for the zeroth-order solution only the application of electric fields normal to the liquid interfaces creates instabilities. As seen from the dependence in Eq. (82), the instability (exponential increase in time) happens in regions where Im $c^{[0]} > 0$.

5 Simulations of the interface instability

(Presented by Walter Villanueva)
An adaptive finite element simulation is implemented to study the electrohydrodynamic stability of two streaming viscous liquids. The flow is tackled as a diffuse-interface problem where the transition between the two fluids has a finite thickness. The fluids are considered viscous and incompressible with variable viscosity, density, and dielectric constant. A phase-field method is considered wherein the system consists of two phases each with distinct constant value and changes rapidly and smoothly in the interfacial region. The flow is governed by the Navier-Stokes equation with added forces due to surface tension, electric field, and gravity. The evolution of the interface is governed by the convective Cahn-Hilliard equation. An equation is derived from free energies of the system and models creation, evolution, and dissolution of diffusively-controlled phase-field interfaces.
The following physical parameters are obtained after nondimensionalizing the equations given in the reference : Reynolds number Re, Capillary number Ca, Bond number Bo, electro-parameter W, Peclet number Pe, viscosity ratio m, and dielectric ratio d. With the parameter values Re=0.001, Ca=0.8, Bo=0.0001, Pe=10000, m=10, d=1.0 which means no electric field is imposed, the flow was

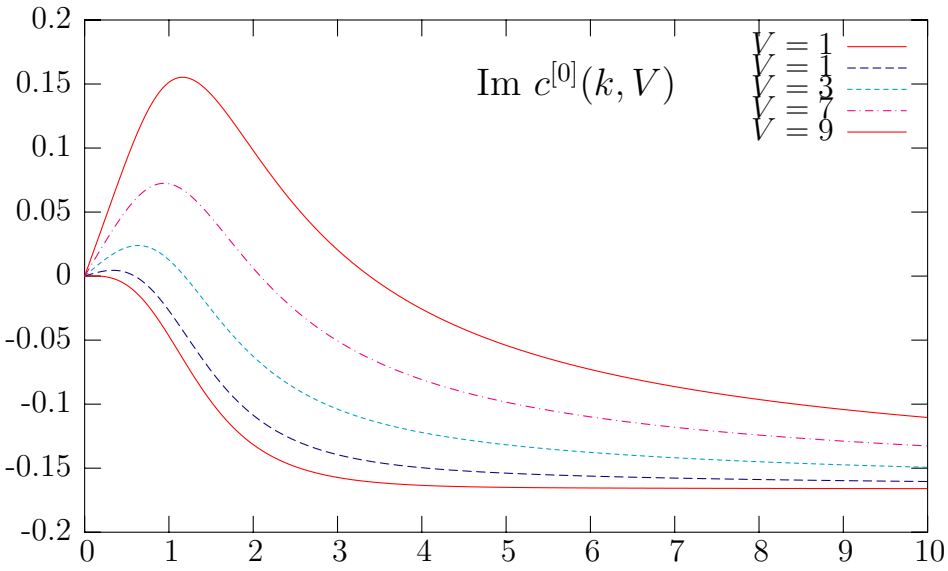

Figure 2: Im $c^{[0]}$ as function of wave number k and applied voltage. An increase in voltage increases the unstable region of long wavelengths (small wave numbers) where the effects of the surface tension are reduced. The curves asymptotically approach each other for very large k as the stabilizing effect of surface tension becomes dominant (provided the voltage remains fixed).

laminar and no signs of instability was observed. A perturbed flow is then added in the streamwise direction with an amplitude of 0.2 and frequency 0.005 and still without electric field. The perturbed flow was damped and the oscillations disappeared.

Finally, an electric field was set directed perpendicular to the flow with d=0.8 and W=0.1. The flow became unstable and the addition of the electric field magnified the perturbation that created a spike with amplitude half of the lower fluid's height.

Figs.5 and 6 show interface before and after the electric field is turned on. Initially flat interface at $t = 0$ becomes deformed as the field is turned on, $t = 2$. Whereas Ref. [1] gives the onset of instability in the linear approximation, the numerical simulations presented here show the nonlinear evolution of the interface beyond the onset, thus complementing the theory.

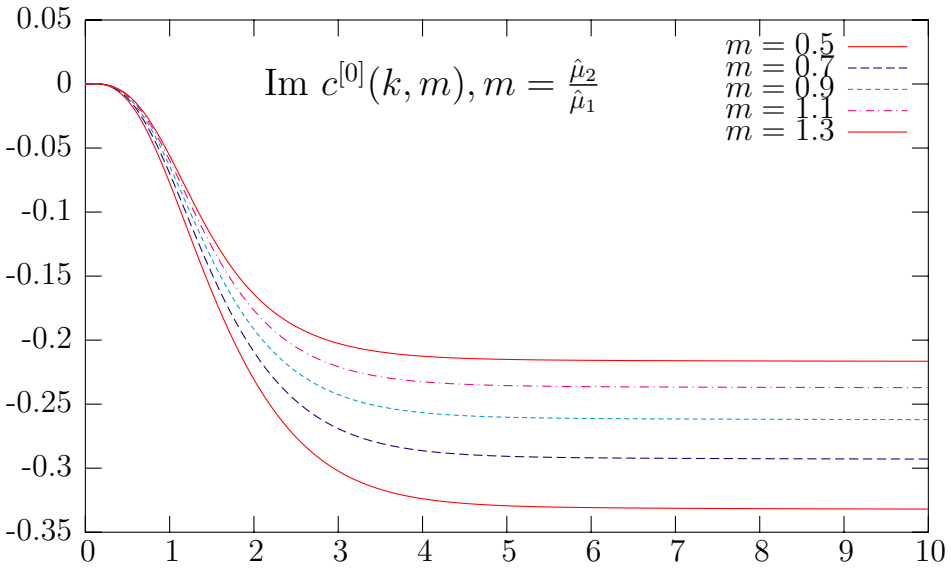

Figure 3: Im $c^{[0]}$ as function of wave number k and viscosity ratio m (and zero electric field). No instability is induced in the zero-order perturbation. The flow, however, becomes relatively *less* stable as m increases, i.e., when the lower liquid becomes more viscous relative to the upper one. Also, for very small wave numbers flow becomes independent of m.

References

[1] G. Goranović, M. P. Sørensen, M. Brøns and Henrik Bruus, *Electrohydrodynamic stability of two streaming viscous liquids inside a microfluidic channel*, in preparation

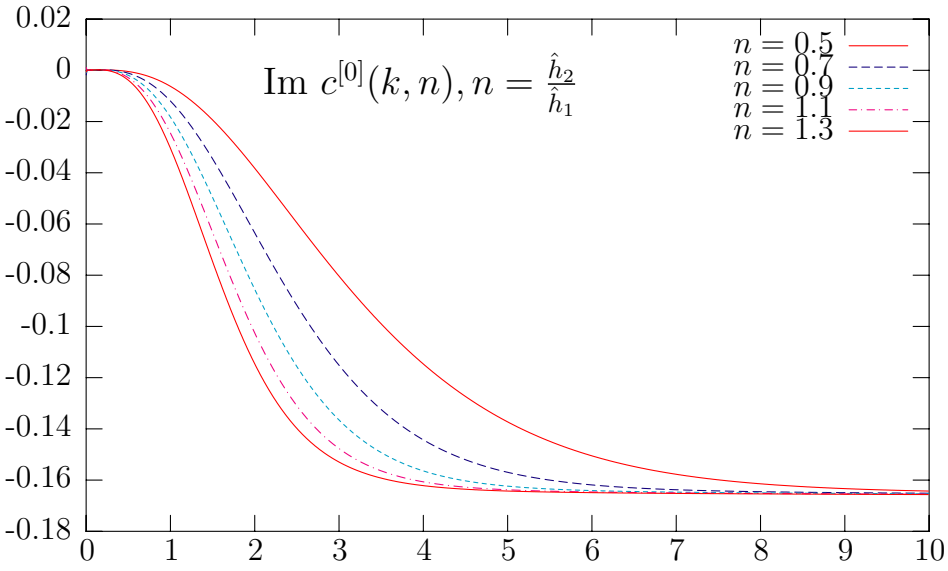

Figure 4: Im $c^{[0]}$ as function of wave number k and thickness ratio n (and zero electric field). No instability is induced in the zero-order perturbation. The flow becomes relatively more stable as n increases, i.e., when the lower layer becomes thicker relative to the upper one. Also, the flow is asymptotically independent of n for very small and large wave numbers.

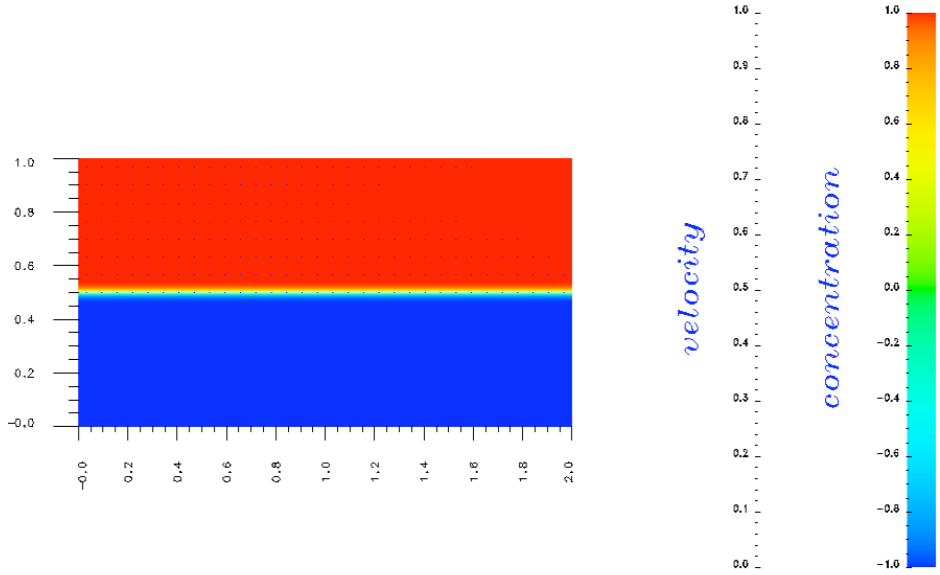

Figure 5: Two-phase flow system with parameters Re=0.001, Ca=0.8, Bo=0.0001, Pe=10000, m=10, d=0.8, and W=0.1 at t=0. The interface is completely flat.

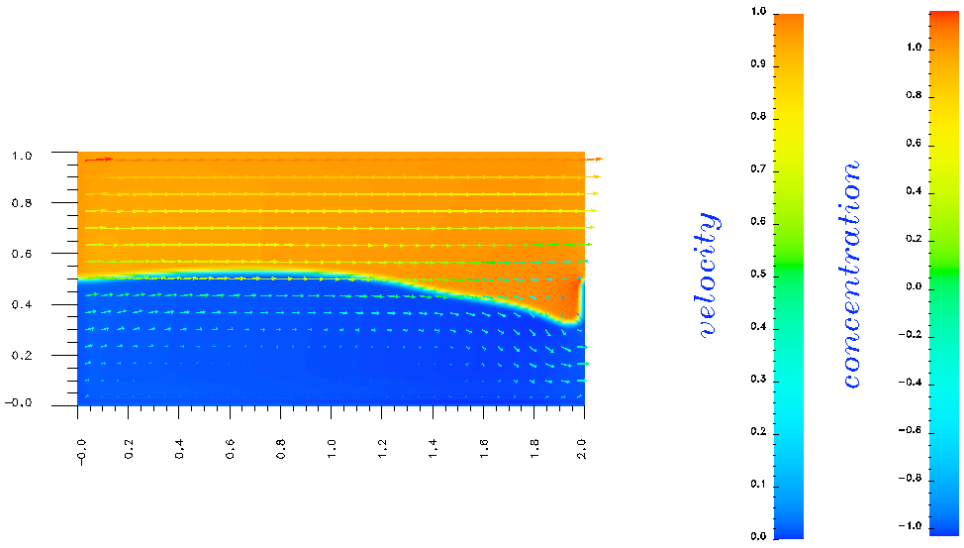

Figure 6: The same system at t=2. Electric field causes the interface instability which eventually becomes a large nonlinear deformation (spike).

Group 5
The reality of the compound solution in magnetohydrodynamics

Axel Brandenburg, Christian Klingenberg, Knut Waagan,
Håvard Huru Bergene, Yuan Lin, Mohammad Motamed,
Thomas Ramstad, Joni Virtanen,

1 Introduction

The equations of magnetohydrodynamics (MHD) are obtained by coupling the Euler equations of gas dynamics and the Maxwell equations of electromagnetism. They describe the flow of a fluid in the presence of magnetic field. For ideal gases, the inviscid MHD equation in one dimension reads

$$\begin{aligned}
\partial_t \rho + \partial_x(\rho v_n) &= 0,\\
\partial_t \rho v_n + \partial_x(\rho v_n^2 + p + \tfrac{1}{2}\mathbf{B}_t^2) &= 0,\\
\partial_t \rho \mathbf{v_t} + \partial_x(\rho \mathbf{v}_t - B_n \mathbf{B}_t) &= 0,\\
\partial_t \rho \mathbf{B_t} + \partial_x(v_n \mathbf{B}_t - B_n \mathbf{v}_t) &= 0,\\
\partial_t E + \partial_x((E + p + \tfrac{1}{2}\mathbf{B}_t^2) v_n - B_n \mathbf{B}_t \cdot \mathbf{v}_t) &= 0,
\end{aligned} \tag{92}$$

where the variables are density ρ, flow velocity $\mathbf{v} = (v_x, v_y, v_z) = (v_n, \mathbf{v_t})$, magnetic field $\mathbf{B} = (B_n, \mathbf{B_t})$, and total energy E. The total energy is substituted by the pressure

$$E = \frac{1}{\gamma - 1} p + \frac{1}{2}\rho v_n^2 + \frac{1}{2}\rho \mathbf{v_t}^2 + \frac{1}{2}\mathbf{B_t}^2, \tag{93}$$

where γ is the adiabatic constant. Note that because of the divergence condition $\nabla \cdot \mathbf{B} = 0$ in 1D, B_n has to be constant, and therefore we consider it as a parameter.

By writing the system (92) in the quasi-linear form $U_t + A\,U_x = 0$, one can see that it has the characteristic velocities

$$\begin{aligned} &\lambda_1 = v - c_f, \lambda_2 = v - c_A, \lambda_3 = v - c_s, \\ &\lambda_4 = v, \\ &\lambda_5 = v + c_s, \lambda_6 = v + c_A, \lambda_7 = v + c_f, \end{aligned} \tag{94}$$

which are the eigenvalues of the Jacobian A. The fast, slow and Alfven velocities are computed as

$$\begin{aligned} c_{f,s} &= \sqrt{\frac{1}{2}\left(\frac{B_n^2 + \mathbf{B_t}^2}{\rho} + a^2\right) \pm \sqrt{\frac{1}{4}\left(\frac{B_n^2 + \mathbf{B_t}^2}{\rho} + a^2\right)^2 - a^2\frac{B_n^2}{\rho}}}, \\ c_A &= \sqrt{\frac{B_n^2}{\rho}}, \end{aligned} \tag{95}$$

where $a = \sqrt{\frac{\gamma p}{\rho}}$ is the sound speed.
Since $c_s \leq c_A \leq c_f$, the real eigenvalues (94) may coincide at certain points, and therefore the MHD equation is a non-strictly hyperbolic system. For example if $B_n = 0$, we get $c_s = c_a = 0$, and v is an eigenvalue of multiplicity 5.

2 Stability of the waves

In a Riemann problem for a hyperbolic system, the initial conditions are discontinuous. the solution of such problems is built from either discontinuities, like shock waves, or rarefaction waves. Due to the non-strict hyperbolicity of MHD equations, the wave structure of the Riemann problem for ideal MHD, governed by 7 waves, is more complicated than for a strictly hyperbolic system; First, the uniqueness of solution is not guaranteed. Second, the system may admit non-regular waves, including compound waves and over-compressive shocks.
We will specifically study the Riemann problem with left state

$$(\rho, v_n, \mathbf{v_t}, B_n, \mathbf{B_t}, p) = (1, 0, [0, 0], 1, [1, 0], 1)\,, \tag{96}$$

and right state

$$(\rho, v_n, \mathbf{v_t}, B_n, \mathbf{B_t}, p) = (0.2, 0, [0, 0], 1, [\cos\alpha, \sin\alpha], 0.2)\,, \tag{97}$$

as initial conditions, which was investigated by Manuel Torrilhon in [4]. Angle α is the initial twist angle of the planes of the magnetic fields. The exact solution for $\alpha = 3.0$ and $\alpha = \pi$ is shown in figure 1.

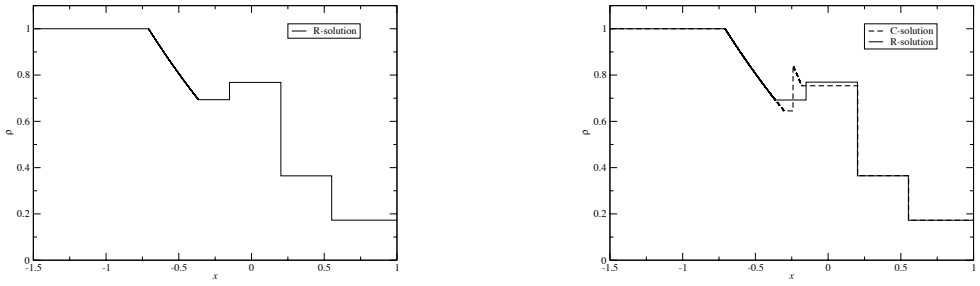

(a) $\alpha = 3.0$ (b) $\alpha = \pi$

Figure 1: Exact solutions of (92,96,97), calculated by Torrilhon [3].

For certain initial data the Riemann problem for ideal MHD does not have a unique solution. In [5], the uniqueness condition has been derived as the following:

Theorem. If for the initial conditions in the non-planar case ($\alpha \neq k\pi, k = 0, 1, 2$), the condition $[[\mathbf{v_t}]] = 0$, or in the coplanar case ($\alpha = \pi$), the condition $0 \neq [[\mathbf{v_t}]] \nparallel [[\mathbf{B_t}]]$ holds, then the MHD Riemann problem has a unique regular solution.

Here, the quantity

$$[[\phi]] := \phi^{(1)} - \phi^{(0)}$$

describes the jump of the fields to right and left of the discontinuity.

From the theorem it follows that the solution of (96) and (97), when $\alpha = \pi$, is not unique since $[[\mathbf{v_t}]] = 0$. In this case the left and right states have magnetic fields in the same plane, and there are two solutions to the Riemann problem, which we will denote the *r-solution* and the *c-solution*, following [4]. The 'r' in *r-solution* stands for *regular* since it is composed of only Lax shocks, rarefactions, rotational discontinuities and a contact discontinuity, all having nice stability properties. The *c-solution*, however, has a *compound* wave (hence the 'c') travelling to the left, where a marginally over-compressive shock is directly followed by a slow rarefaction. For $\alpha \neq \pi$ there is only one solution, U_α to the Riemann problem (96), (97), and as $\alpha \to \pi$, U_α approaches the r-solution. Hence the *c-solution* is unstable to arbitrarily small perturbations of B out of the plane.

Therefore one might suggest that the *c-solution* does not have physical significance.

However, we have assumed that there is no viscosity, which is an approximation. In the viscous equation the momentum equations are modified as follows:

$$\begin{aligned} \partial_t \rho v_n + \partial_x(\rho v_n^2 + p + \tfrac{1}{2}\mathbf{B}_t^2) &= \frac{2}{3}\nu\partial_x(\rho\,\partial_x v_n), \\ \partial_t \rho \mathbf{v_t} + \partial_x(\rho \mathbf{v}_t - B_n \mathbf{B}_t) &= \nu\partial_x(\rho\,\partial_x \mathbf{v_t}), \end{aligned} \tag{98}$$

If $\nu > 0$ the *c-solution* will be stable under small perturbations in phase space, including perturbations of B out of the plane. However this stability region shrinks with ν, until it disappears at $\nu = 0$, see [2].

When doing numerical simulations of the inviscid equations, one also gets more complex behaviour than the inviscid analysis suggests. For $\alpha = \pi$, all the schemes we are aware of pick the *c-solution*. However, if α is slightly perturbed, at coarse grids the schemes will still tend to the *c-solution*, and begins to converge to the unique regular solution only when the grid is refined sufficiently. Since all the schemes add viscosity in a certain sense, it is plausible that the analysis of the viscous equation might provide some explanation for this. For coarser resolution the numerical viscosity is higher, so it is as though the data are within the stability region of the *c-solution* until we refine, and thereby reduce viscosity, sufficiently.

3 Solving the inviscid MHD equations

To solve the inviscid one dimensional MHD equations (92) numerically we used the Staggered Central Scheme by Tadmor and Nessyahu [1]. The scheme is 2. order i01 Devilś Haircut.mp3n time and space. Already on the second day of the workshop we were able to run a few test runs with an existing two-dimensional code written by Knut Waagan for $\alpha \neq \pi$.

The only modifications needed was specifying the initial conditions, and setting the dimensions to $n \times 1$. We were able to reproduce the convergence behavior discussed by Torrilhon in [4]. For coarse grids the solution is "c-like", and for finer grids the solution approaches the correct r-solution.

Since the code was two-dimensional it was quite time consuming to run on finer grids ($>$ 10000 grid points). The goal was to run on very fine grids ($>$ 100000 grid points), so we stripped the 2nd dimension from the code, giving a purely one-dimensional code. Then the code ran about 10 times faster. The code running on a 1.6 GHz portable computer ran 10000 grid points to time t=0.4 in a couple of hours, while 50000 grid points required about 24 hours. In order to run on even finer grids we started parallelizing the code.

3.1 Parallel version

The parallelization was done using domain decomposition. Assuming that we have N processors (and domains) numbered by $i \in [0, N-1]$ and n total grid points. The the domain of processor i have $n_i = n/N$ grid points. The division is integer, and in case the modulo is nonzero, each processor with rank less than the modulo get one more grid point. In addition the grid has two[1]ghost cells on both sides of the domain. The ghost cells are set by communicating the corresponding cells

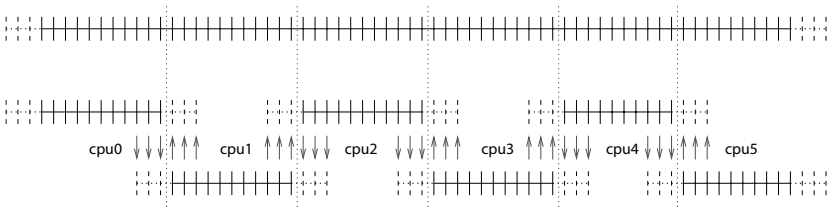

Figure 2: An example of domain decomposition of a system with $n = 64$ grid points distributed to $N = 6$ processors. Arrows show the direction of communication.

from the neighbouring domains. Figure 2 shows an example for $n = 64$ and $N = 6$. The arrows shows the direction of communication. If the ghost cells lie outside the boundaries of the total grid they are set using Neumann boundary conditions. The communications are done using MPI which is widely available and may run on both massively parallel computers and workstation clusters.

[1]Actually we use three ghost cells to avoid communicating twice each time step.

The parallelization was done just in time to run on 100000 grid points before last preparations for the next days final presentations. Using 32 2,6GHz processors on the Horseshoe cluster in Odense (Denmark) the running time was less than 1 hour.

3.2 Results

In figure 3 we have plotted the density, ρ and the y-component of the magnetic field B_y for different number of grid points using (96,97) and $\alpha = 3.0$. Note that for coarse grids we get a solution that is similar to a *c-solution*, and that for the finer grids we approach the analytic *r-solution*.

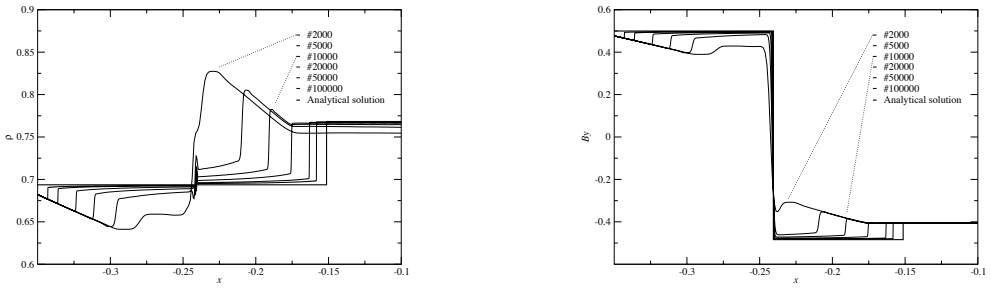

Figure 3: The transition from a "c-like" solution towards the exact r-solution for $\alpha = 3.0$.

3.3 Numerical stability of the r-solution

For $\alpha = \pi$ we were not able to get the r-solution at all numerically. But as a step towards achieving that, we decided to sample the r-solution at some time, and use it as the initial condition for the Nessuahu-Tadmor scheme. In order to do so we obtained from M. Torrilhon his calculation of the exact solution to the Riemann problem (96)-(97). The simulation did not simply evolve the r-solution as one would expect. Instead the left-going rotational discontinuity broke up into several new structures that eventually interacted with the slow shock - Hence the self-similarity of the r-solution was destroyed. We believe that this failure is due to a general difficulty in resolving rotational discontinuities numerically, since similar phenomena could be observed for other Riemann problems consisting only of a rotational discontinuity. There seemed to be some analogy with the issue of resolving shear waves in hydrodynamics. However this observation does not

contradict the presence of rotational discontinuities in numerical solutions of other Riemann problems. In that case they emerge in a stable fashion out of other structures. It is possible that some kind of smoothing of the initial rotational discontinuity would solve this issue.

3.4 1-D simulation using the Pencil code

Although the pre-existing Pencil code was able to provide the necessary tool for the numerical computing, it – as a fully three-dimensional – was a bit supernumerary for our purposes. Namely, as we needed only one-dimensional analysis and only certain 1-D related operations, the inclusion of un-needed extra dimensions and complex numerical algorithms were slowing down the simulations unnecessarily. Thus, we decided to write a new, lighter 1-D code basing on the Pencil code in order to reduce computing time in the forthcoming simulation runs.

The "dimension reduction" was performed so that one of the group leaders as well as one of the members started to work on the pre-existing code using CVS [2] for keeping track of changes and dealing with (and avoiding, as much as possible) conflicting modifications of the source codes. This approach turned out to be successful, and at the end of the week we had managed to do nearly all the modifications needed to have 1) modules for the physical interactions and properties, 2) mathematical formulas for needed derivatives and other operations, and 3) data handling and visualization procedures turned or rewritten to work in the 1-D scheme.

Taking into account the limited amount of time for working within the frames of the workshop, the (re)writing of the whole simulation code package was, obviously, too wide a project to be completed in order to have a working and tested code for the rest of the groups, so the contribution of the coding part of the work group to the overall research of the group remained minor. On the pedagogical side, on the other hand, this part of the project was very fruitful: getting in touch with larger scale coding projects and learning to use certain development and code writing tools effectively, together with seeing alternative uses for some familiar tools, was very instructing.

As for the future, there is still more work to do in order to get the code fully working in every aspects, including not only the dimensional conversion and rewriting of the code, but also testing and documentation as well; this project is very likely to continue beyond the workshop.

[2] Concurrent Versioning System, see `https://www.cvshome.org/`

3.5 Regular and compound solutions in the 1D viscous case

We investigate numerically solutions to the MHD problem where the RHS of Eq. (92) do not vanish and the momentum equations will take the form of Eq. (98). Initially a regular shock is applied, and it is the aim of this section to look at the non-uniqueness in solutions for different values of α and ν, hence the angle between $\mathbf{B}_t$ before and after the shock and the viscosity.
In the case where we have the least viscosity the solutions have more numerical noise due to the discretization of the grid. We used grid sizes of hence 20000 and 50000 grid points in the x-direction due to the scheme described previously. The runs were carried out on a single CPU with the serial version of the Pencil Code and the results are shown in the figures below.

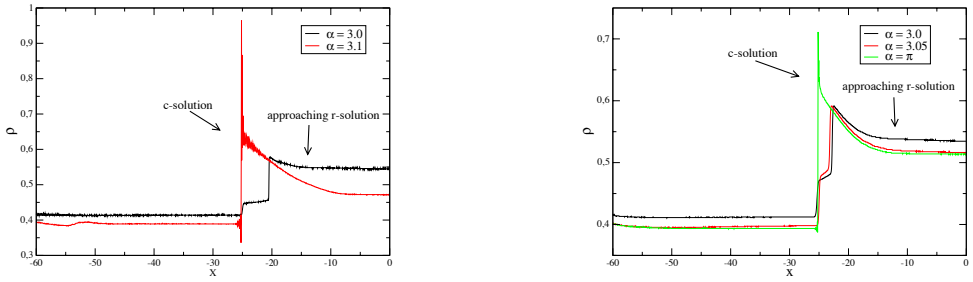

Figure 4: Numerical solutions with $\nu = 0.002$ and $\nu = 0.005$ with different α. The runs are done with 50000 grid points and took several hours on a single CPU.

In the results we see that for $\alpha = \pi$ and close to $\alpha = \pi$ the solution is compound like, while in the case of $alpha < 3.1$ the solutions tend towards a regular wave.

References

[1] Jorge Balbás, Eitan Tadmor, and Cheng-Chin Wu. Non-oscillatory central schemes for one- and two-dimensional MHD equations. I. *J. Comput. Phys.*, 201(1):261–285, 2004.

[2] Heinrich Freistühler and Tai-Ping Liu. Nonlinear stability of overcompressive shock waves in a rotationally invariant system of viscous conservation laws. *Comm. Math. Phys.*, 153(1):147–158, 1993.

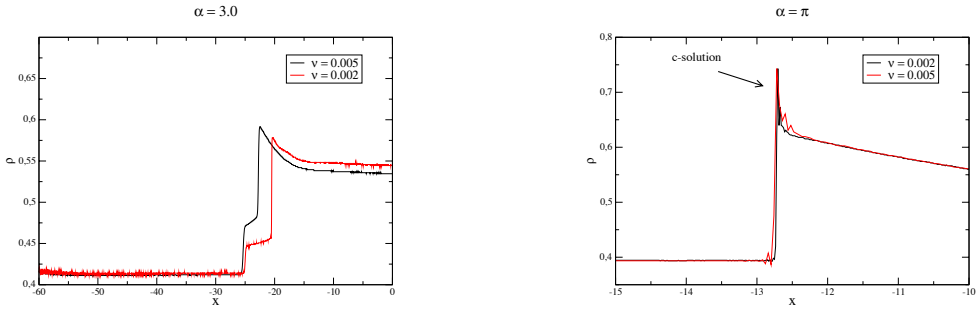

Figure 5: Numerical solutions with $\alpha = 3.0$ in the upper figure and $\alpha = \pi$ in the lower with different ν. The solutions for $\alpha = 3.0$ case is clearly tending towards a regular wave solutions.

[3] M. Torrilhon. Exact solver for riemann problems of ideal magnetohydrodynamics. Technical report, Research report 2002-06. Seminar for Apllied Mathematics. ETH Zürich, 2002.

[4] M. Torrilhon. Non-uniform convergence of finite volume schemes for Riemann problems of ideal magnetohydrodynamics. *J. Comput. Phys.*, 192(1):73–94, 2003.

[5] M. Torrilhon. Uniqueness conditions for riemann problems of ideal magnetohydrodynamics. *J. Plasma Physics*, 69(1):253–276, 2003.

Group 6a
A Monte Carlo approach to DNA-breathing with two bubbles

Mikael S. Hansen , Jonas N. Pedersen , Tomáš Novotný

1 Introduction

Double stranded (ds) DNA is made of nucleotide base pairs adenine (A) binding only to thymine (T) and guanine (G) binding only to cytosine (C) via two and three hydrogen bonds, respectively. This difference in the number of bonds leads to a difference in melting temperature with $T_m^{AT} \sim 20-70°\mathrm{C}$ and $T_m^{GC} \sim 70°\mathrm{C}$ [1]. At body temperature the typical structure of dsDNA is that of the well-known (right-handed) α-helix but when increasing the temperature the strands can dissociate and form bubbles as illustrated in Fig. 1.

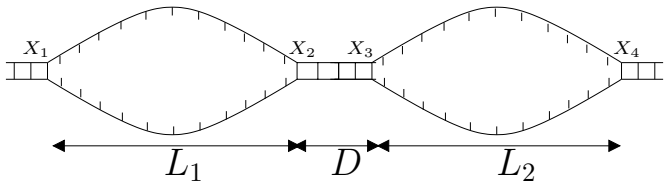

Figure 1: Sketch of a two-bubble scenario in a homopolymer as considered in this article. Endpoints should be considered as clamped such that a complete separation of the DNA strands cannot occur.

Recently it has become possible to study the dynamics of individual bubbles in short ($\sim 30-40$ base pairs) segments of designed DNA using fluorescence correlation spectroscopy [1] and the method is currently being extended to longer

segments. This will allow experimental studies of dynamically more interesting situations, e.g. the two-bubble scenario presented in this article.[1]
The bubble dynamics is determined by a local bond-breaking mechanism and a global entropic loop closing cost (due to a reduction in the number of configurations as the ends of the strands are forced to meet and form loops) [7].

2 The model

We model dsDNA as a sequence of N base pairs each of which can be either formed (zipped) or broken (unzipped). As initial conditions we take endpoints X_1, X_2 for the first bubble and X_3, X_4 for the second bubble where $X_1 < X_2 \leq X_3 < X_4$ shown in Fig. 1. The length $L_i, i = 1, 2$, is the number of broken base pairs in bubble i. The distance between the bubbles is denoted D.
We assume that only base pairs at the zipper forks, $X_1, .., X_4$, can either unzip, or the neighboring base pairs can zip, i.e. no new bubbles are initiated during the simulation.[2] The bubble dynamics are now given by rates, $r_i^{-(+)}$, for zipping (unzipping) at X_i. We have generic rates

$$\begin{aligned} r_1^+ = r_2^+ &= ku\left(\frac{L_1+1}{L_1+2}\right)^c \\ &= ku\left(\frac{X_2-X_1}{1+X_2-X_1}\right)^c, \quad \text{(unzipping)} \qquad (99) \\ r_1^- = r_2^- &= k, \qquad \text{(zipping)} \qquad (100) \\ r_3^+ = r_4^+ &= ku\left(\frac{L_2+1}{L_2+2}\right)^c \\ &= ku\left(\frac{X_4-X_3}{1+X_4-X_3}\right)^c, \quad \text{(unzipping)} \qquad (101) \\ r_3^- = r_4^- &= k, \qquad \text{(zipping)} \qquad (102) \end{aligned}$$

also used in Ref. [4] to study the evolution of a single bubble. Here k is the zipping rate of a single base pair and $u = \exp(-\Delta E_{\text{break}}(T)/k_BT)$ the statistical weight associated to the breaking of an additional base pair. We use $\Delta E_{\text{break}}(T_m) = 0$ such that $u = 1$ is the weight at melting temperature. The last factor in the unzipping rates stems from the entropic cost $(1+L)^{-c}$ of making the single strands meet to

[1] For practical reasons it will be more interesting to consider the heteropolymer situation. We return briefly to this later.

[2] This is a reasonable assumption due to a high bubble initiation cost $\Delta E_{\text{bubble}} \sim (7-12)\, k_BT$ yielding the cooperativity parameter $\sigma_0 = \exp(-\Delta E_{\text{bubble}}/k_BT) \sim 10^{-3} - 10^{-5}$.

form a bubble of length L. The constant c is set to $c = 3 \times 0.588$ (see [4] and references therein).[3]
Boundary conditions have to be handled separately. When the bubbles are at the boundaries of the DNA

$$\begin{aligned} r_1^+ &= 0, \qquad X_1 = 1 \\ r_4^+ &= 0, \qquad X_4 = N \end{aligned} \tag{103}$$

and when the bubbles have a common boundary base pair

$$r_2^+ = r_3^+ = \frac{ku}{2\sigma_0} \left(\frac{(L_1+1)(L_2+1)}{L_1+L_2+2} \right)^c, \quad X_2 = X_3 \tag{104}$$

where $\sigma_0 \sim 10^{-5} - 10^{-3}$ is a coorporativity parameter expressing how costly it is to initiate a new bubble due to the breaking of the non-local helix structure(see footnote 10).
Remark: To construct the rates Eqs. (99)-(104) we assume the detailed balance condition to be satisfied by our system. This is a sufficient (but not necessary) condition for the system to reach equilibrium eventually.[4]
It is possible to formulate the problem in terms of a master equation

$$\dot{P}(\{X_1, X_2, X_3, X_4\}) = \hat{L} P(\{X_1, X_2, X_3, X_4\}), \tag{105}$$

where $P(\{X_1, X_2, X_3, X_4\})$ is the probability of finding the DNA in a configuration $\{X_1, X_2, X_3, X_4\}$ and $\hat{L}$ is a linear operator[5]. A master equation approach has been used for both a single bubble [7] and its interaction with single stranded binding proteins [2]. However this approach is not suitable for more bubbles where the larger number of degrees of freedom makes even the formulation of a master equation intractable. Following Ref. [4] we instead use the Gillespie (Monte Carlo) algorithm presented in the next section.

3 The Gillespie algorithm

Given an initial configuration, $\{X_i^0\}$, we want to simulate how the two bubbles evolve in time. To do this we apply the Gillespie algorithm introduced in 1973 as a stochastic approach to the study of chemical reactions. In this section we briefly describe the algorithm [6].

[3] P-G. de Gennes' *Scaling Concepts in Polymer Physics*, Cornell Univ. Press, Ithaca (1979). c is the (Flory) scaling exponent for the radius of gyration of a 3-dimensional self-avoiding random walk.

[4] For more information about detailed balance see papers by work group 3 directed by T. Ala-Nissilä.

[5] This corresponds to a simple Markov process, i.e. there is no memory in the system.

With two bubbles there are eight ways of updating the system, that is, zipping or unzipping at one of the four zipper forks. We assume that the statistical weight for a given event, μ, to happen in a time interval $[t, t+\delta t$ is $r_\mu \delta t$. Here r_μ are the rates defined in the previous section, i.e. $\mu = (i, +/-), i = 1, \ldots, 4$. As some of the rates depend on the length of a bubble, the probability for something to happen depends on the configuration, $\{X_i\}$, of the system at time t.
The idea is now the following [6]:
What is the probability that nothing happens in the time interval $[t, t+\tau]$ *and* in the following interval $[t+\tau, t+\tau+d\tau]$ an event of type μ happens?
This probability is the so-called *joint probability density*

$$P(\tau, \mu)d\tau = P_0(\tau) r_\mu d\tau. \tag{106}$$

To determine the probability $P_0(\tau)$ that no event happens within $[t, t+\tau]$, this interval is divided into K pieces of length $\epsilon = \tau/K$. The probability that nothing happens in the first subinterval $[t, t+\epsilon]$ is then

$$\prod_\mu [1 - r_\mu \epsilon] = 1 - \sum_\mu r_\mu \epsilon + \mathcal{O}(\epsilon^2). \tag{107}$$

Treating the remaining intervals similarly gives

$$\begin{aligned} P_0(\tau) &= [1 - \sum_\mu r_\mu \epsilon + \mathcal{O}(\epsilon^2)]^K \\ &= [1 - \sum_\mu r_\mu \tau/K + \mathcal{O}(K^{-2})]^K. \end{aligned} \tag{108}$$

Taking the limit $K \to \infty$ and reinserting in Eq. (106) we end up with

$$P(\tau, \mu) = r_\mu \exp[-\sum_\mu r_\mu \tau]. \tag{109}$$

At time t the system is in a configuration $\{X_i\}$ and the update is done as follows:
i) Rates r_μ are calculated using Eqs. (99)-(104).
ii) Generate a pair of random numbers (τ, μ) distributed according to $P(\tau, \mu)$ in Eq. (109). [6]
iii) Advance the time $t \to t + \tau$ and update the configuration $\{X_i\}$ according to the randomly chosen event μ.
The steps *i*)-*iii*) are repeated until the bubbles merge *or* one bubble disappears in which case we obtain the one-bubble scenario of [7]. We record the stop time and

[6] How this is done using random numbers generated from a uniform distribution is shown in Appendix 6.

the final configuration $\{X_i\}_{final}$ and a new run is initiated using the same initial condition.
Remark: An advantage of the Gillespie algorithm (as opposed to the standard Metropolis algorithm) is that the system changes at every update. There are no rejection steps involved — even if the system gets "stuck" in long-lived state it only takes one update in the Gillespie algorithm to move on (instead we have a long waiting time at no computational cost).

4 Simulations

In all simulations the initial conditions are $X_1 = 250$, $X_2 = 350$, $X_3 = 400$, $X_4 = 500$ and the length of DNA segment is $N = 1000$.

4.1 A single time series

With the stochastic approach we can study both ensemble properties and single time series. Examples of the latter are given in Fig. 2 and Fig. 3 showing the death of one bubble and the two bubbles merging, respectively.

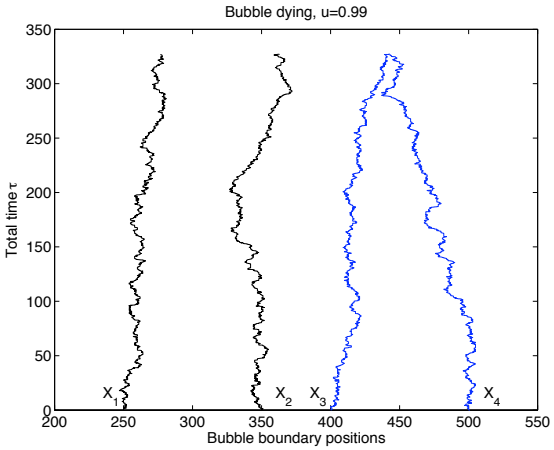

Figure 2: A single time series where the right bubble dies (and the simulation terminates).

4.2 Statistics: Merging/dying times

Turning to the ensemble properties we have made series of $200,000$ runs for different parameter values. The simulation runs until a bubble dies or the bubbles

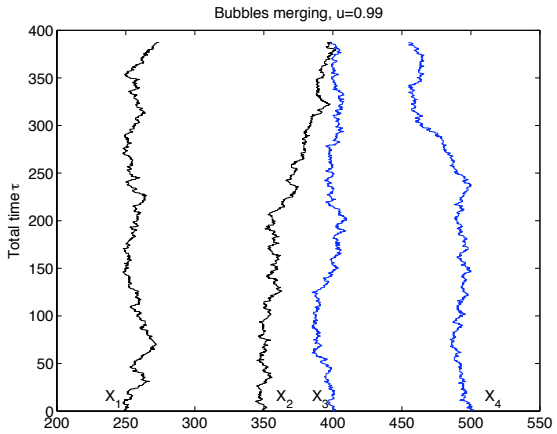

Figure 3: A single time series where the two bubbles merge (and the simulation terminates).

merge. The final configuration and the stop time τ_{die} or τ_{merge} are then recorded. The results for the probability densities of the two kinds of the stop time are shown as histograms in Fig. 4.

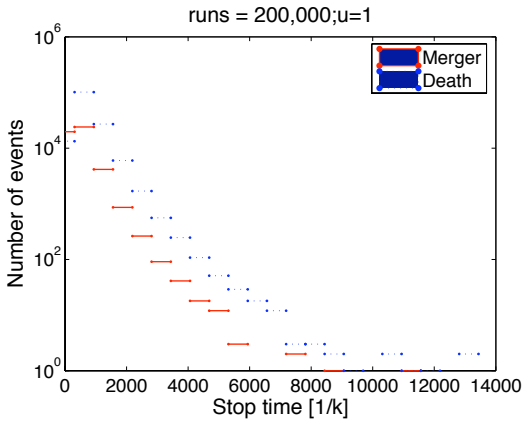

Figure 4: Distribution of merger (red full lines) and death (blue dashed lines) times for $200,000$ runs and $u = 1$.

5 Discussion and outlook

We see from Fig. 4 that the probability densities behave roughly exponentially for intermediate times (for large times the statistics is insufficient to make any

conclusions). This would allow one to define characteristic "life-times" of the two bubble configuration after which a bubble dies or the bubbles merge. It would be interesting to study the behavior of these times as functions of initial conditions and other parameters.
In experiments the presence of two bubbles - used as initial condition in our simulations - is an extremely unlikely event due to the loop initiating factor $\sigma_0 \sim 10^{-5} - 10^{-3}$ [3]. More interesting is the case of a heteropolymer, where the DNA-string is made of sequences of different base pairs (AT or GC) giving position dependent Boltzmann factors u_{AT}, u_{GC}. This is easy to implement in the Gillespie scheme introduced above and one can now envision experiments done at temperatures where $u_{AT} > 1$ while $u_{GC} < 1$.
Extending to the heteropolymer case is of broad interest, e.g. in the case of intron positions in dsDNA (non-coding parts) which is claimed to be linked to the presence of domains melting at different temperatures [5]. This is however still an issue of debate.

6 Appendix: Probability distribution

Following Ref. [6] we briefly present how random numbers τ and μ can be constructed using numbers drawn from a uniform distribution.
Let $P_c(\tau')$ be some continuous probability *density* function, e.g. $P_c(\tau')d\tau$ is the probability for finding a τ within the interval $[\tau', \tau' + d\tau]$. The probability *distribution* function is defined as

$$F_c(\tau_0) = \int_{-\infty}^{\tau_0} P_c(\tau')\mathrm{d}\tau', \tag{110}$$

which is the probability of some τ being less than τ_0. To get a random τ according to P_c given some random number $R \in [0, 1]$ drawn from the uniform distribution we have to invert $F_c(\tau) = R$.
Using $P_c(\tau) = \sum_\mu P(\tau, \mu)$ of Eq. (109) with $\tau > 0$ and inverting we get

$$\tau = \frac{1}{\sum_\mu r_\mu} \ln(\frac{1}{R}). \tag{111}$$

In the discrete case

$$F_d(\mu_0) = \sum_{\nu=1}^{\mu_0} P_d(\nu), \tag{112}$$

is the probability of having $\mu \leq \mu_0$. Inversion given some random number $R \in [0, 1]$ drawn from the uniform distribution is now requiring that $F_d(\mu - 1) < R < F_d(\mu)$.

Using $P_d(\mu) = \int P(\tau, \mu) \mathrm{d}\tau$ the random event μ is determined by

$$\sum_{\nu=1}^{\mu-1} r_\nu < R \sum_{\nu=1}^{N} r_\nu \leq \sum_{\nu=1}^{\mu} r_\nu. \tag{113}$$

References

[1] G. Altan-Bonnet, A. Libchaber, and O. Krichevsky. Bubble dynamics in double-stranded dna. *Phys. Rev. Lett.*, 90:138101, 2003.

[2] T. Ambjörnsson and R. Metzler. Coupled dynamics of dna-breathing and binding of proteins that selectively bind to single-stranded dna. *arXiv:q-bio.BM/0411053*, 2004.

[3] T. Ambjörnsson and R. Metzler. Binding dynamics of a single stranded dna binding proteins to fluctuating bubbles in breathing dna. *J. Phys: Cond. Matt.*, 17:1841–1869, 2005.

[4] S. K. Banik, T. Ambjörnsson, and R. Metzler. Stochastic approach to dna breathing dynamics. *Europhys. Lett.*, 2004.

[5] E. Carlon, M. L. Malki, and R. Blossey. Exons, introns, and dna thermodynamics. *Phys. Rev. Lett.*, 94:178101, 2005.

[6] D. T. Gillespie. A general method for numerically simulating the stochastic time evolution of coupled chemical reactions. *J. Comp. Phys*, 22:403–434, 1976.

[7] A. Hanke and R. Metzler. *J. Phys. A: Math. Gen.*, 36:L473, 2003.

Group 6b
Membranes

Group leader: Dr. Ilpo Vattulainen
Group: MSc Måns Elenius, MSc Jari Jalkanen,
MSc Ivan Degtyarenk

1 Motivation

Many problems in biophysics present several different time- and length scales. From the atomic level, with lengths of a few angstroms (atom size) and times of femtoseconds (time associated with bond vibrations) to macrolevel with seconds and micro/millimetres [5]. To resolve physical questions, one needs to combine experimental and theoretical (computational) means that complement each other and focus on different scales in time and space. It is exceedingly difficult to obtain detailed information of nano-sized domains through experiments, while atomic-scale simulations can gauge atomic-scale phenomena in a rather straight-forward manner using classical molecular dynamics simulations. The main problem concerns the time and length scales in the middle: how to look at systems whose sizes are of the order of 50-100 nm, and time scales of the order of 100-1000 ns. These scales are beyond those that are doable by atomistic simulations; yet they are also (in part) beyond the scales that can be probed by experiments. To understand processes over these scales, one has to resort to multiscale modelling which are based on coupling different techniques to each other in a systematic manner. Hence gaining insight into the properties of complex soft matter systems over a multitude of different scales. In a wide context, the main problem is to understand how processes in complex bio systems can be modelled with sufficient accuracy, such that only the key features of the problem are included.

2 Simulating Model

Biological membranes, relatively large living structures, with interfaces composed of two lipid monolayers whose hydrophobic sides are attached to each other such that their contact with water is minimized. The opposite polar head group of lipids are oriented towards water to maximize their contact with water phase. Membranes found in living cells are very complicated and consists of hundreds of different lipids and other fats. They also contain carbohydrates and proteins having more or less known contributions to the functions of a living cell. A schematic picture of a cell membrane can be found in Figure 1. Simulation models of cell membranes are of course far less complicated, usually taking into account a maximum of three different kinds large biological molecules in addition to water. The modelling molecules in the simulations are also simplified out of necessity; an ordinary lipid contains well over 100 atoms. Different levels of coarsening are used in different models everything from grouping atoms identified as a functional unit in the molecule to modelling the complete molecule as a single particle.

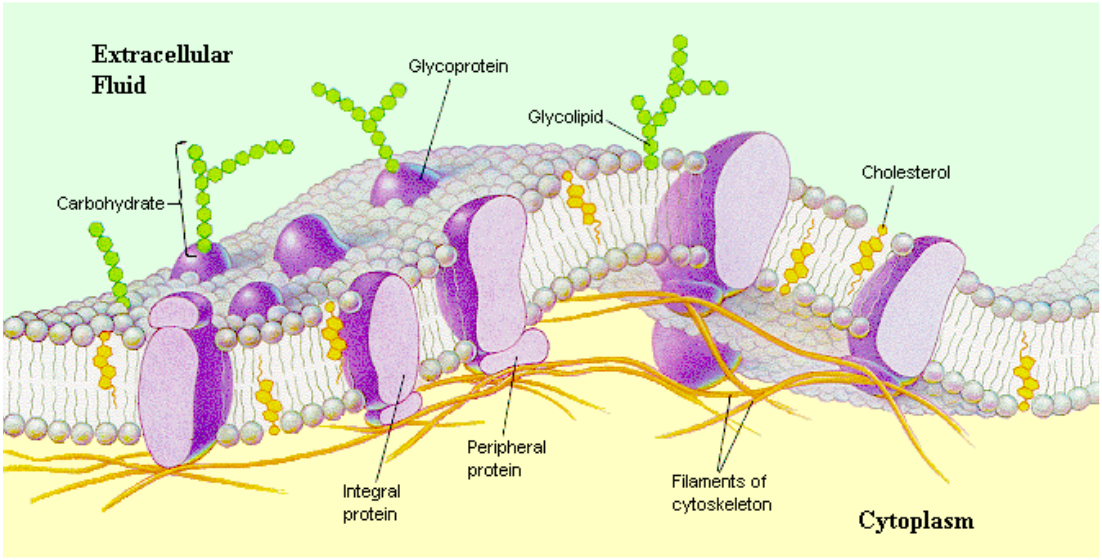

Figure 1: Schematic picture of cell membrane (adopted from Human Biologyby Daniel Chiras).

3 Task and Methodology

The task set forward to the group was to try to find novel ways of simulating membranes on a length scale of 100 nm and timescales of ?s. As guidance we discussed with group leader Dr. Ilpo Vattulainen and read papers provided by him. It probably should be mentioned, that none of us have had heavy background in that field, before the workshop. The group work alternated between reading papers and discussing ideas. Hence we came up with some ideas that we later found in papers. Some of these are still mentioned below to better reflect the work performed in the group. We kept our discussion to improvement of molecular level simulations that still keep some of the molecular structure. We made this choice mainly for two reasons. First we all felt that we had more knowledge in atomic and molecular models and second Ilpo's group in TKK, Finland is working with the extreme coarsening of modelling each molecule as a single atom and performing the complete simulation in two dimensions, ref. [3].

4 Ideas

The following list contains the ideas put forward by the group members during the work. They are colour coded so that blue red means done before (put together with a reference), blue means partly done and green means not done to our knowledge.

4.1 Integrate the electric interactions in the pair potential (and tabulate)

Several simulation schemes seem to incorporate cut offs for both interatomic (Van der Waals) interactions and electronic interactions. Still it seems like they are kept different from each other and also that they are analytically calculated in each step. We believe that there is room for improvement by integrating the electrical interactions and the interatomic interactions and tabulate the two to reduce calculations. Since this calculation is right in the kernel of the computation it may increase performance significantly.

4.2 Identify slow and fast dynamics, integrate them in different ways

This has been done in ref. [1].

4.3 Try to get completely rid of the shortest timescale (atomic vibrations)

This has been done in ref. [2].

4.4 Increase masses of the light atoms (hydrogen) to increase timescale

We have not seen this done in any membrane simulation. Probably the reason is that it is by far most useful when you have explicit hydrogen in your model and all models we have seen for membrane simulations are on a far coarser level than that. Still there might possibly be some situations where this is useful. Mass increasing allows using larger time step in MD simulations.

4.5 Try to integrate the water in the interactions in between the other particles

This has been done in reference [3].

4.6 Simulate the lipid tails using only one or two particles

We have not seen this level of coarsening, only several particles in each tail or one particle for the complete molecule. There might be a problem to find a good spherically symmetric interatomic potential that gives a reasonable behaviour for this model. But it would definitely decrease calculations from the other models we have seen that are trying to retain some of the molecular structure.

4.7 Use rigid molecules, fix angles/bonds

The idea is to treat the molecules as rigid bodies but still keep atoms or coarsened parts of the molecule for the force calculations. This would get rid of all intramolecular interactions including torsions and angles and would hence decrease the force calculations significantly. Still it seems a bit counter intuitive that this model should yield anything both new and correct, but you never know until you have tried.

4.8 Discuss the use of MD/MC/kinetic MC - Use lattices?

We discussed how one could benefit from using molecular dynamics and Monte Carlo in different ways and also tried to find schemes for kinetic Monte Carlo, but

we did not get very far on this. There is an interesting paper, ref [4], where they get better results from molecular dynamics than from Monte Carlo.

4.9 Model a monolayer using "water" on one side and "oil" on the other side

This has most probably been done but we have not seen it in any of the papers we have read. In ordinary membrane you have, as stated above, two layers of lipids with their hydrophilic end pointing out of the membrane towards the surrounding water and the hydrophobic end pointing inwards towards the hydrophobic tails of the other layer. The idea here is to model an oil-like substance, simply a particle type liking the hydrophobic tails and despising the hydrophilic heads, on the "tail-side" of the membrane so that you don't have to model both layers of the membrane. This will of course only save around half of the computational cost, as compared to the orders of magnitude needed to reach the goals in the field, but still it might prove an improvement.

References

[1] Shelley, J.C.; Shelley M.Y.; Reeder R.C.; Bandyopadhyay S.; Klein M.L.; Simulations of Phospholipids Using a Coarse Grain Model, J. Phys. Chem. B, 2001, 105, 9785-9792.

[2] Groot, R.D.; Rabone K.L.; Mesoscopic simulation of cell membrane damage, morphology and rupture by non-ionic surfactants, Biophysical Journal, 2001, 81, 81725-736.

[3] Murtola, T.; Falck E.; Patra M.; Kartunen M.; Vattulainen I.; Coarse-grained model for phospholipid/cholesterol bilayer, J. Chem. Phys. 2004, 121, 18.

[4] Shelley, J.C.; Shelley M.Y.; Reeder R.C.; Bandyopadhyay S.; Klein M.L.; A Coarse Grain Model for Phospholipid Simulations, J. Phys. Chem. B, 2001, 105, 4464-4470.

[5] Vattulainen, I. and Kartunen M.; Chapter 29 of Handbook of Theoretical and Computational Nanotechnology, 2005, American Scientific Publishiers, edited by Rieth M. and Schommers W.

Group 6c
DNA knots

V. Borodin, M.Ganchenkova, M.Elenius

1 Physical problem

DNA chains can be considered as nanostrings with the length measured in terms of base pairs it contains, L. They are grown initially as linear structures, but when they become long enough, string entanglement and knot formation are possible. When the ends of a chain are put together, ideally one would obtain a closed ring (or, more precisely, a figure topologically identical to a ring). However, where a string is sufficiently long and have freedom to move before the end joining, it can become knotted. The sections of the whole chain occupied by "localized" knots behave differently from the "unknot" sections, which for some purposes may be considered as a favourable circumstance and for others - not. In order to make simulations that explicitly treat the knots on a specified DNA chain, one needs first of all some means to numerically localize the knots and to identify the lengths of segments occupied by knots.

2 Computational task

To propose an idea of efficient and reliable algorithm for locating knots and separating the whole chain into regions that can be treated as belonging to knots and the sections that can be treated as knot-free.

2.1 Underlying problems

1. The first problem in reaching the final aim is an internal inconsistency. Indeed, a knot in a purely topological sense is a closed manifold. On the other hand, knot localization means separation of the whole chain into separate unclosed segments, which can have no knots in topological sense.

2. Even if we introduce a trick that tells us that a knot is fully confined within a specified string section, it is not clear how to define the knot size in a way, which is free from intuitive considerations.

3 Possible solution

A DNA chain is naturally discretized, which means that its most natural representation is not by a continuous rope but rather by a string of beads, where each individual 'bead' marks the position of individual base pair. We may also assume that the neighbouring beads are connected by imaginary 'bonds', and define that the spatial orientation of a bond defines the local chain orientation. It is additionally convenient to introduce bond directions, so that any bead terminates exactly two bonds so that one bond is terminated with its start and another - with its end. The geometry of a chain is assumed strictly fixed.
The whole algorithm might then consist of two major parts

1. Topological. First of all, it makes sense to specify how many knots are present. Since the initial configuration is closed, this can be done using purely topological means (e.g. by calculation of Jones or HOMFLY polynomial). If the total number of non-linked knots is N, it meant that it is possible to make at least N cuts that will separate the total string into "separate" sections, each having exactly one "sub-knot" (in a more complicated case it might be possible to separate linked "sub-knots" as well). The question remains, where to make such cuts. However, after the cutting is done, knot localization procedure is intuitively clear - one should tear off the beads at the loose ends of a 'one-knot' section as long as the knot remains identifiable by topological means.

2. Geometrical. The key point in the algorithm is the localization of "cut points". To achieve this aim, we should be able to uniquely decide for any fixed finite-length string of beads, whether it contains a knot, or not. This cannot be done by purely topological means, so some geometrical assumptions are inevitable, guided by purely intuitive feelings about what might be considered as "isolated knot". In particular, we propose to introduced for any finite-length string a "tangent infinity closure" (TIC), that is - we demand that any finite-length string section must be continued infinitely at the ends exactly in the directions of its boundary bonds (conserving the bond orientation). Such an infinite structure is now a uniquely identified knot.

Then we can proceed in the following way.

1. Select an arbitrary bond. No matter, where it is, its TIC is equivalent to that of an unknot.

2. Add bonds in positive direction until TIC of the whole than remains that of the unknot. Fix the "positive" boundary at the bead, whose addition changes the topology properties of TIC.

3. Remove bonds one by one, starting from the initial one until TIC equivalence of the resulting bond to the unknot is restored. Fix the last removed bead as a "negative" boundary. The length of the section between a negative and the next positive boundary can be defined as knot length in TIC approximation, while the distance between a positive and next negative boundary (as measured in positive direction of the chain) - as a length of an unknot section.

Now we can take the bond emerging from the "positive boundary" bead and repeat the cycle, until all the knots are identified. The procedure is unique for N >1, but for a unique knot it is possible to cut the chain in many places compatible with TIC approximation. Since we are interested in knot localization, it makes sense to identify ALL possible unknot section and cut the longest one, which will automatically define the shortest knot. However, to say, whether the knot is localized, or not one needs additional purely geometrical criteria, based either on the comparison of knot and unknot lengths, or on 3D confinement of knot and unknot sections, or both. However, as far as the separation into knot and unknot sections is done, this remains a straightforward task.

4 Conclusion

We propose the basic idea of a possible algorithm for separation of a closed knotted string of beads into sections with individual knots. In practical cases (an evident example is a "knot inside knot") this idea may require expansion, but the main principle most probably works, if properly expanded. However, technical realization requires more programming efforts that one might afford during the time span of the workshop.

Participants of Computational Problems in Physics – CPiP 2005 Helsinki, May 23 - 27, 2005

Achim, Cristian Vasile
Laboratory of Physics, TKK
cva@fyslab.hut.fi

Ala-Nissilä, Tapio
Laboratory of Physics, TKK
tapio.ala-nissila@tkk.fi

Ali-Löytty, Simo
Institute of Mathematics
Tampere University of Technology
simo.ali-loytty@tut.fi

Ambjörnsson, Tobias
NORDITA
ambjorn@nordita.dk

Bakke, Jan Öystein
Institut for fysikk, NTNU
janoiste@phys.ntnu.no

Bergene, Håvard Huru
Institut for fysikk, NTNU
huru@phys.ntnu.no

Bohr, Dan
MIC, DTU
dab@mic.dtu.dk

Borodin, Vladimir
RRC Kurchatov Institute
v.borodine@mail.ru,
borodin@dni.polyn.kiae.su

Brandenburg, Axel
NORDITA
brandenb@nordita.dk

Bruus, Henrik
MIC, DTU
bruus@mic.dtu.dk

Byckling, Mikko
Institute of Mathematics, TKK
mbycklin@cc.hut.fi

Bäck, Thomas
NuTech Solutions
baeck@nutechsolutions.de

Cornaglia, Pablo
CEA-Saclay
cornagli@drecam.saclay.cea.fr

Degtyarenko, Ivan
Laboratory of Physics, TKK
Ivan.Degtyarenko@hut.fi

Dzugutov, M
NADA, KTH
mik@nada.kth.se

Eirola, Timo
Institute of Mathematics, TKK
timo.eirola@tkk.fi

Elenius, Måns
NADA, KTH
elenius@nada.kth.se

Engquist, Björn
NADA, KTH
engquist@nada.kth.se

Flindt, Christian
MIC, DTU
cf@mic.dtu.dk

Ganchenkova, Maria
Laboratory of Physics, TKK
mgc@fyslab.hut.fi

Goranovic, Goran
MEMPHYS
University of Southern Denmark
goran@memphys.sdu.dk

Gripenberg, Gustaf
Institute of Mathematics, TKK
gustaf.gripenberg@tkk.fi

Gylfadottir, Sigridur Sif
Laboratory of Physics, TKK
ssg@fyslab.hut.fi

Hansen, Mikael Sonne
DTU
m.s.hansen@mat.dtu.dk

Hansson, Anders
Avdelning Matematik, KTH
anhan@math.kth.se

Havu, Paula
Laboratory of Physics, TKK
pah@fyslab.hut.fi

Havu, Ville
Institute of Mathematics, TKK
Ville.Havu@tkk.fi

Hochbruck, Marlis
Heinrich-Heine-Universität, Düsseldorf
marlis@am.uni-duesseldorf.de

Holmgren, Sverker
Department of Information Technology
Uppsala universitet
sverker@tdb.uu.se

Huhtanen, Marko
Institute of Mathematics, TKK
Marko.Huhtanen@tkk.fi

Jalkanen, Jari
Laboratory of Physics, TKK
jhj@fyslab.hut.fi

Jauho, Antti-Pekka
MIC, DTU
antti@mic.dtu.dk

Jensen, Mads Jakob
MIC, DTU
mjj@mic.dtu.dk

Junes, Heikki
Low Temperature Laboratory, TKK
heikki.junes@tkk.fi

Juntunen, Mika
Institute of Mathematics, TKK
mojuntun@cc.hut.fi

Järvi, Tommi
Accelerator Laboratory
University of Helsinki
tommi.t.jarvi@helsinki.fi

Karttunen, Mikko
Laboratory of Computational
Engineering, TKK
karttune@lce.hut.fi

Katsoulakis, Markos
University of Massachusetts
markos@math.umass.edu

Klingenberg, Christian
Institut für angewandte Mathematik
Universität Wuerzburg
klingenberg@
mathematik.uni-wuerzburg.de

Koponen, Ismo T
Department of Physical Sciences
University of Helsinki
ismo.koponen@helsinki.fi

Koponen, Laura
VTT Microsensing / TKK
lkoponen@cc.hut.fi

Krupchyk, Katsiaryna
Department of Mathematics
University of Joensuu
krupchyk@joyx.joensuu.fi

Kuusela, Esa
Laboratory of Physics, TKK
ehk@fyslab.hut.fi

Lassen, Benny
Mads Clausen Institute
The University of Southern Denmark
benny@mci.sdu.dk

Laurila, Teemu
Laboratory of Physics, TKK
teemu.laurila@hut.fi

Lin, Yuan
Department of Mechanics, KTH
yuan@mech.kth.se

Lomholt, Michael
NORDITA
mlomholt@nordita.dk

Loubenets, Alexei
NADA, KTH
alexei@nada.kth.se

Martin-Löf, Anders
Department of Mathematics
Stockholm University
andersml@math.su.se

Mataich, Mustapha
Institute of Mathematics, TKK
mustapha.mataich@tkk.fi

Metzler, Ralf
NORDITA
ralf.metzler@nordita.dk

Morlanes, Jose Igor
Institute of Mathematics, TKK
morlanes@mappi.helsinki.fi

Motamed, Mohammad
NADA, KTH
mohamad@nada.kth.se

Nevanlinna, Olavi
Institute of Mathematics, TKK
Olavi.Nevanlinna@tkk.fi

Nieminen, Risto
Laboratory of Physics, TKK
rni@fyslab.hut.fi

Novotny, Tomas
Nano-Science Center
University of Copenhagen
novotny@fys.ku.dk

Ostermann, Alexander
Institut für Mathematik
Universität Innsbruck
alexander.ostermann@uibk.ac.at

Pedersen, Jonas
Department of Physics
Lund University
jonas.pedersen@fysik.lu.se

von Pfaler, Jan
Institute of Mathematics, TKK
Jan.von.Pfaler@tkk.fi

Punkkinen, Olli
Laboratory of Physics, TKK
olli.punkkinen@hut.fi

Pursiainen, Sampsa
Institute of Mathematics, TKK
spursiai@cc.hut.fi

Puska, Martti
Laboratory of Physics, TKK
martti.puska@hut.fi

Ramstad, Thomas
Institut for fysikk, NTNU
thomas.ramstad@phys.ntnu.no

Rantala, Tapio
Semiconductor Physics Laboratory
Tampere University of Technology
tapio.rantala@tut.fi

Runborg, Olof
NADA, KTH
olofr@nada.kth.se

Marko Rusanen
Laboratory of Physics, TKK
Marko.Rusanen@hut.fi

Schweitzer, Julia
Heinrich-Heine-Universität, Düsseldorf
Schweitzer@am.uni-duesseldorf.de

von Schwerin, Erik
NADA, KTH
schwerin@kth.se

Stenberg, Rolf
Institute of Mathematics, TKK
Rolf.Stenberg@tkk.fi

Szepessy, Anders
NADA, KTH
szepessy@math.kth.se

Tunturivuori, Lasse
Laboratory of Physics, TKK
ltu@fyslab.hut.fi

Urboniene, Vidita
Vilnius University
vidita.alisauskaite@ff.vu.lt

Vattulainen, Ilpo
Laboratory of Physics, TKK
Ilpo.Vattulainen@hut.fi

Villanueva, Walter
Department of Mechanics, KTH
walter@mech.kth.se

Virtanen, Joni J.P.
Tuorla Observatory
University of Turku
jonvir@utu.fi

Voigt, Axel
Research Center Caesar
voigt@caesar.de

Vrublevskaja, Oksana
Institute of Physics, Lithuania
oksana@ar.fi.lt

Waagan, Knut
Center of Mathematics for Applications
University of Oslo
knut.waagan@cma.uio.no

(continued from the back cover)

A480 Ville Havu , Jarmo Malinen
Approximation of the Laplace transform by the Cayley transform
December 2004

A479 Jarmo Malinen
Conservativity of Time-Flow Invertible and Boundary Control Systems
December 2004

A478 Niko Marola
Moser's Method for minimizers on metric measure spaces
October 2004

A477 Tuomo T. Kuusi
Moser's Method for a Nonlinear Parabolic Equation
October 2004

A476 Dario Gasbarra , Esko Valkeila , Lioudmila Vostrikova
Enlargement of filtration and additional information in pricing models: a Bayesian approach
October 2004

A475 Iivo Vehviläinen
Applyining mathematical finance tools to the competitive Nordic electricity market
October 2004

A474 Mikko Lyly , Jarkko Niiranen , Rolf Stenberg
Superconvergence and postprocessing of MITC plate elements
January 2005

A473 Carlo Lovadina , Rolf Stenberg
Energy norm a posteriori error estimates for mixed finite element methods
October 2004

A472 Carlo Lovadina , Rolf Stenberg
A posteriori error analysis of the linked interpolation technique for plate bending problems
September 2004

HELSINKI UNIVERSITY OF TECHNOLOGY INSTITUTE OF MATHEMATICS
RESEARCH REPORTS

The list of reports is continued inside. Electronical versions of the reports are available at *http://www.math.hut.fi/reports/* .

A486 Hanna Pikkarainen
A Mathematical Model for Electrical Impedance Process Tomography
April 2005

A485 Sampsa Pursiainen
Bayesian approach to detection of anomalies in electrical impedance tomography
April 2005

A484 Visa Latvala , Niko Marola , Mikko Pere
Harnack's inequality for a nonlinear eigenvalue problem on metric spaces
March 2005

A482 Mikko Lyly , Jarkko Niiranen , Rolf Stenberg
A refined error analysis of MITC plate elements
April 2005

A481 Dario Gasbarra , Tommi Sottinen , Esko Valkeila
Gaussia Bridges
December 2004

ISBN 951-22-7875-8
ISSN 0784-6460